

# Global synthetic seismograms using a 2-D finite-difference method

Dunzhu Li,<sup>1</sup> Don Helmberger,<sup>1</sup> Robert W. Clayton<sup>1</sup> and Daoyuan Sun<sup>2</sup>

<sup>1</sup>Seismological Laboratory, California Institute of Technology, Pasadena, CA, 91125, USA. E-mail: lidunzhu@gmail.com

<sup>2</sup>Department of Earth Sciences, University of Southern California, Los Angeles, CA, 90089, USA

Accepted 2014 February 6. Received 2014 February 5; in original form 2013 September 20

## SUMMARY

Two-dimensional (2-D) finite-difference (FD) synthetics, which fill the gap between fast 1-D analytic synthetics and time-consuming full 3-D synthetics in our ability to model seismograms, have been used in many studies. We address several issues involving 2-D FD methods in generating global synthetic seismograms. These include: (1) interfacing point source excitation for earthquakes with 2-D FD methods; (2) out-of-plane spreading corrections and (3) reducing the spherical Earth to the flattened models. The first issue is tackled using two methods, a ‘transparent source box’ approach and a moment tensor excitation approach, where each has its own advantages. Moreover, our ‘source box’ excitation does not have the late-time drift problem that occurred in previous studies. The out-of-plane geometric spreading correction is accounted for by estimating the ray parameter and applying a post-simulation filter to 2-D synthetics. Finally, parameters of the Earth-flattening transformation are discussed and validated. The effectiveness of this method is demonstrated by comparing our synthetics with frequency–wavenumber summation, normal-mode and 3-D spectral-element synthetics.

**Key words:** Body waves; Computational seismology; Wave propagation.

## 1 INTRODUCTION

Our knowledge of the structure of the Earth has been greatly improved through the development of global seismic tomography. These models are routinely used in global centroid moment tensor (GCMT) solutions ([globalCMT.org](http://globalCMT.org)) and, more recently, in synthetic seismogram predictions, such as the spectral-element method (SEM, Komatsitsch & Tromp 1999; Tromp *et al.* 2010). Here, as a motivation for our study, we compare how well the tomographic model works for a deep (578 km) earthquake beneath the Russian–China border. The geometry is illustrated in Fig. 1(a) with a typical tomographic model shown in Fig. 1(b). A tangential record section from USArray aligned on the S phase is constructed by stacking the data every 0.8° in distance, shown in Fig. 1(c). Synthetic predictions are shown in Fig. 2 as downloaded from the Shake Movie website (<http://global.shakemovie.princeton.edu>). The synthetics have been stacked in the same way as in the data and filtered to the accurate band for synthetics (17 s and longer in this case). When stacked, we can easily detect secondary arrivals that are reflected by the uppermantle discontinuities, as shown in Fig. 1(c). A comparison of 1-D and 3-D synthetics indicates that the waveform shapes for most arrivals are similar as shown in Fig. 3. In short, 1-D synthetics agree with the 3-D SEM tomographic model synthetics better than either model fits the data. Thus the tomographic models can be refined by adding waveform modelling.

Synthetic seismograms are the main tools in modelling the complexities in the seismic body waves. In 3-D wave simulations, the space–time discretization leads to a scaling of computational cost with the 4th power of seismic frequency, which makes simulations

especially challenging for high resolution. Moreover, the available data may not be enough to constrain a 3-D model. And sometimes the 2-D model assumption, which assumes the elastic parameters are invariant in the direction perpendicular to the great circle propagation plane, is a good approximation for many problems. Thus, 2-D media assumption is often used in waveform modelling, which later can be checked against the SEM results as in Chen *et al.* (2007).

To compare synthetics with data, the point dislocation earthquake source and out-of-plane spreading, which are 3-D features, need to be considered. There are many existing methods for so-called ‘2.5-D simulation problem’, for example, 2-D finite difference (FD) in Cartesian coordinates (with a correction operator for out-of-plane spreading) (Vidale & Helmberger 1987); 2-D pseudospectral method in cylindrical coordinates (with out-of-plane spreading correction, Furumura *et al.* 1998; Wang *et al.* 2001); axisymmetric FD (Jahnke *et al.* 2008); axisymmetric SEM (Nissen-Meyer *et al.* 2007). The axisymmetric modelling takes into account the out-of-plane spreading automatically, and by coupling *P-SV* system and *SH* system, and using Fourier expansion in transverse direction, axisymmetric modelling can also handle non-axisymmetric momentum tensor (Toyokuni & Takenaka 2006). However, if we are interested in a non-axisymmetric model, such as a slab near the source region, axisymmetric methods may not be suitable.

Here, we will focus on the 2-D FD simulation in Cartesian coordinates, a method which has been studied extensively. To interface with an earthquake source in 2-D simulation, Vidale & Helmberger (1987) used a source box approach, which was first proposed by Alterman & Karal (1968), but the synthetics have artificial late-time drifts. Coutant *et al.* (1995) used a momentum approach, which is

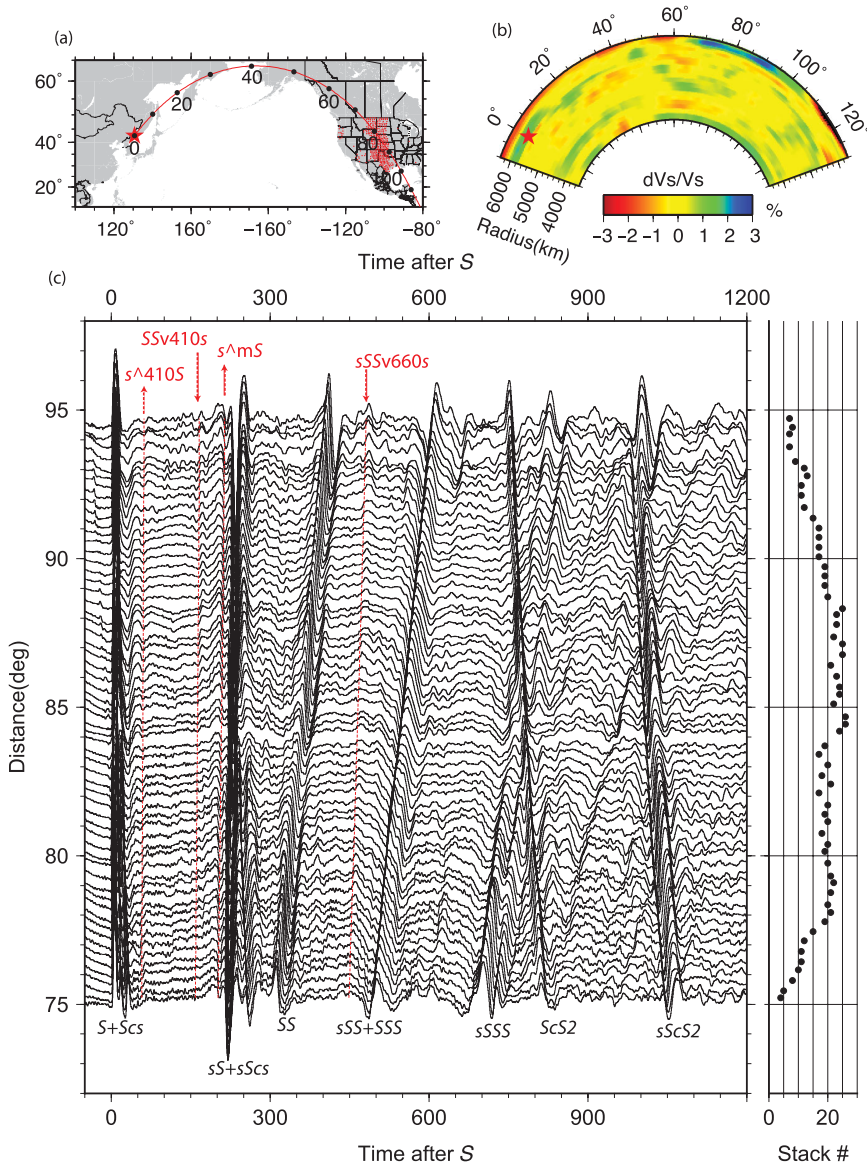


**Figure 1.** A USArray  $SH$  stacked record section from a deep earthquake. (a) The 2010 February 18 event (red star) was recorded by the USArray (red dots). The red line indicates one great-arc path (azimuth =  $37^\circ$ ) and the numbers indicate the distance in degrees. (b) GyPSum S-wave tomography model (Simmons *et al.* 2010) along this path. (c) Stacking of the  $SH$  displacement seismogram aligned on the  $S$  phase. The bin size is  $0.8^\circ$  with a  $0.4^\circ$  overlap, and the number of traces with each bin is dotted on the right-hand panel. The main phases are labelled at the bottom. Several clear minor phases interacting with 410 or 660 km discontinuity are labelled red at the top. Note that  $s410S$  is the precursor of  $sS$  phase, and  $SSv410S$  is the pegleg of  $SS$  phase, following the name convention of Taup Toolkit (Crotwell *et al.* 1999).

not compatible with double-couple solution normally assumed in modelling earthquakes. To address these source excitation issues, we first consider the relationship between 2-D and 3-D simulations (the out-of-plane spreading). Next, we show some improvements and detailed analysis of two source excitation methods.

Our approach involves several approximations with the far-field assumption, the out-of-plane spreading correction and the application of Earth-flattening transformation for non-layering spherical media. A comparison of our synthetics with data from the above event is shown in Fig. 4. The traveltimes fits well, but because of the lack of attenuation in our current code, the amplitude and waveform of upper-mantle phases (e.g.  $sSSS$ ) become difficult to compare. However, in many applications, convolving with a  $t^*$  operation or changing the source-time function can take into account the effective attenuation for a particular phase quite well.

Our goal is not to include all the complexity generally attributed to the Earth, but to develop a pragmatic tool in waveform modelling of global body wave seismograms, in particular some waveform segments. We show that our approach is sufficient for many waveform modelling applications.

## 2 METHODS

### 2.1 3-D spreading

The relationship between point source and line source seismograms has been discussed in detail in recent textbooks, for example, Chapman (2004). We will illustrate this using an explosion source in a fluid whole space.

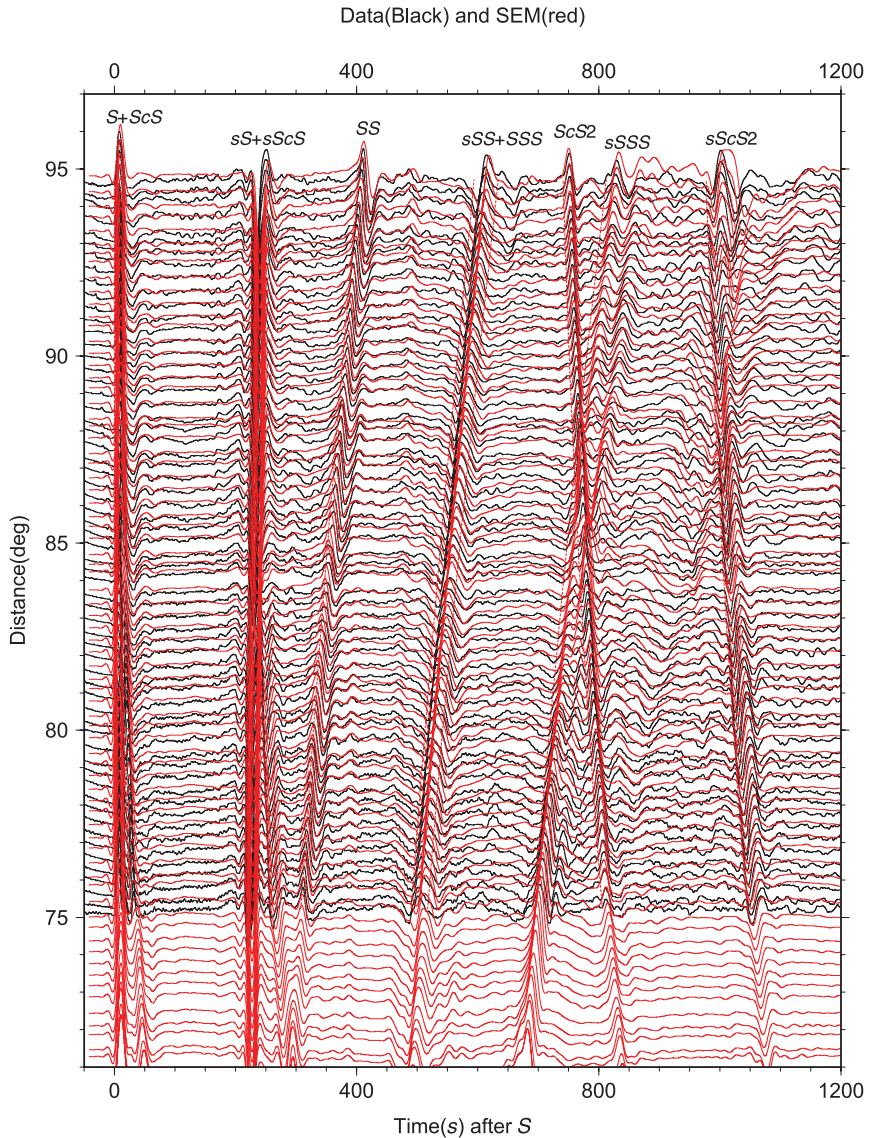


**Figure 2.** Comparison of data (black) and SEM synthetics (red) for the  $SH$  displacement. The data are the same as shown in Fig. 1. The SEM synthetics are stacked the same way as the data.

For a point source at the origin, the solution (denoted as  $V_{3D}$ ) follows the usual form

$$V_{3D}(x, y, z, t) = \frac{1}{R_3} \delta(t - R_3/\alpha), \quad (1)$$

where  $\alpha$  is  $P$ -wave velocity, and  $R_3 = \sqrt{x^2 + y^2 + z^2}$  is the source–receiver distance,  $\delta$  is Dirac delta function.

Following Aki & Richards (1980, p. 226), a line source (along  $y$ -direction) solution (denoted as  $V_{2D}$ ) can be obtained by integrating point source solutions along this line

$$\begin{aligned} V_{2D}(x, z, t) &= \int_{-\infty}^{\infty} V_{3D}(x, y, z, t) dy \\ &= \frac{2H(t - R/\alpha)}{\sqrt{t^2 - R^2/\alpha^2}} \\ &= \frac{2H(t - R/\alpha)}{\sqrt{t + R/\alpha}\sqrt{t - R/\alpha}} \\ &\approx \sqrt{\frac{2\alpha}{R}} \frac{H(t - R/\alpha)}{\sqrt{t - R/\alpha}}, \end{aligned} \quad (2)$$

where  $R = \sqrt{x^2 + z^2}$  is the distance for the 2-D problem,  $H$  is the Heaviside step function, and the last approximation holds because the main contribution to  $V_{2D}$  is from the singularity at  $P$ -arrival time  $t = R/\alpha$ .

Hence, if we have a line source seismogram, we can obtain point source seismogram at the same position by

$$V_{3D}(x, 0, z, t) = \frac{1}{\pi} \sqrt{\frac{p}{2x}} \frac{d}{dt} \left[ \frac{1}{\sqrt{t}} * V_{2D}(x, z, t) \right], \quad (3)$$

where  $p = x/R\alpha$  is the geometric ray parameter for the  $P$  arrival.

For a general 2-D media, a similar result for each individual arrival can be obtained by ray theory (Cerveny 2001)

$$V_{3D}(x, 0, z, t) = \frac{1}{\pi} \sqrt{\frac{1}{2F}} \frac{d}{dt} \left[ \frac{1}{\sqrt{t}} * V_{2D}(x, z, t) \right], \quad (4)$$

Mode(Black) and SEM(red)

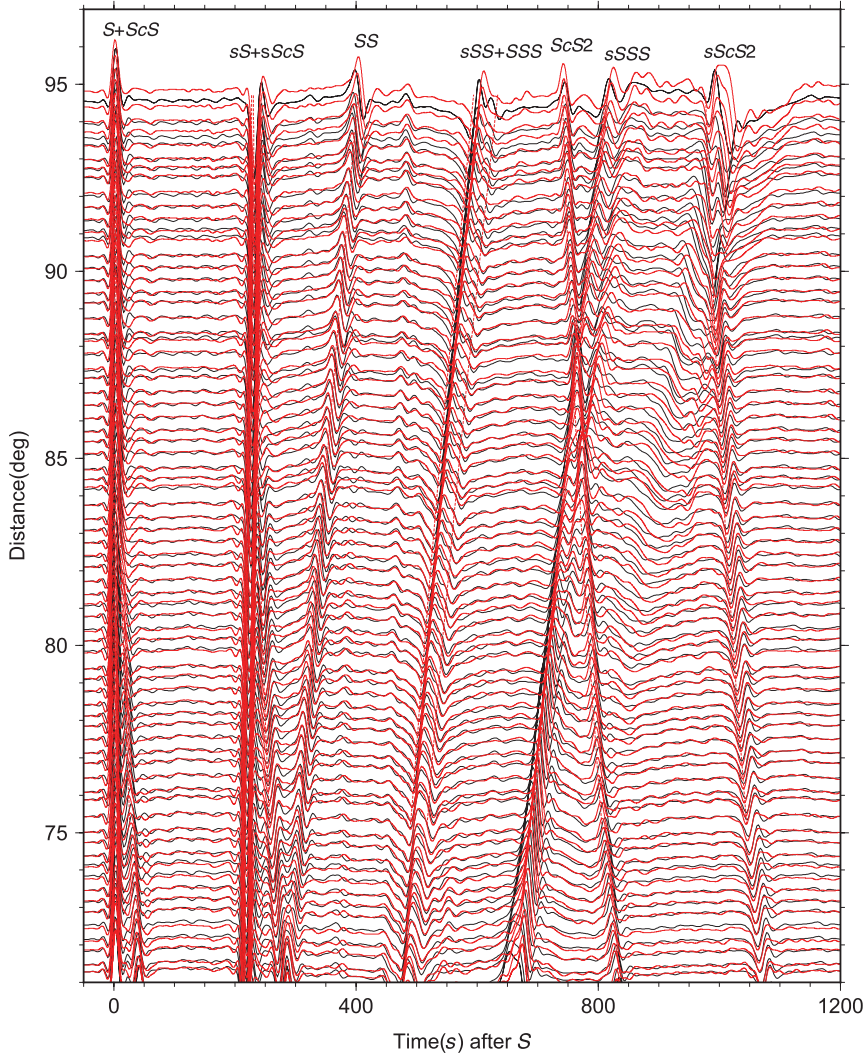


**Figure 3.** Comparison of the 1-D mode summation synthetics (black) and the SEM synthetics (red) for the  $SH$  displacement. The mode synthetics are stacked the same way as the data.

where the factor  $F = \int_{\text{ray}} v \, ds$  is an integration of wave travelling velocity  $v$  along the ray path  $ds$ . In a layered media, eq. (4) reduces to eq. (3) because

$$F = \int_{\text{ray}} v \, ds = \int_{\text{ray}} \frac{v}{\sin \theta} \sin \theta \, ds = \int_{\text{ray}} \frac{1}{p} \, dx = \frac{x}{p}, \quad (5)$$

where  $\theta$  is the incident angle, and  $p$  is constant along the ray by Snell's law.

However, note that on one seismogram,  $p = p(t)$  is different for the various seismic phases. Miksat *et al.* (2008) showed that using ray tracing to calculate the  $F$  factor for each phase, line source seismogram can be corrected to obtain the point source seismogram, phase by phase. However, ray tracing is complicated and processing phase by phase is cumbersome. Instead, we assume eq. (5) holds for typical global simulations, with  $p$  the ray parameter observed at receiver side. This is a good approximation if the velocity perturbation is small (typical tomographic model), or the strong heterogeneity is far from receivers and is small in size. Then, eq. (3) will hold. We will show the correction  $\sqrt{p(t)}$  in eq. (3) can be constructed automatically without using ray tracing. This allows the correction

of a whole seismogram without using different windows for the various arrivals.

To construct  $\sqrt{p}$ , we first estimate the ray parameter  $p(t)$ . Because

$$p = \frac{ik_x}{i\omega} \quad (6)$$

in the frequency ( $\omega$ ) and wavenumber ( $k_x$ ) domain, where  $i = \sqrt{-1}$ ,  $ik_x$  corresponds to a differential operator in the  $x$  direction and  $1/i\omega$  corresponds to an integral operator in time, thus operationally

$$p(t)[\dots] \rightarrow -\frac{d}{dx} \int [\dots] dt. \quad (7)$$

Indeed, applying this to  $V_{2D}$  in previous example

$$\begin{aligned} -\frac{d}{dx} \int \left[ \frac{H(t - R/\alpha)}{\sqrt{t - R/\alpha}} \right] dt &= \frac{x}{R\alpha} \left[ \frac{H(t - R/\alpha)}{\sqrt{t - R/\alpha}} \right] \\ &= p \left[ \frac{H(t - R/\alpha)}{\sqrt{t - R/\alpha}} \right]. \end{aligned} \quad (8)$$

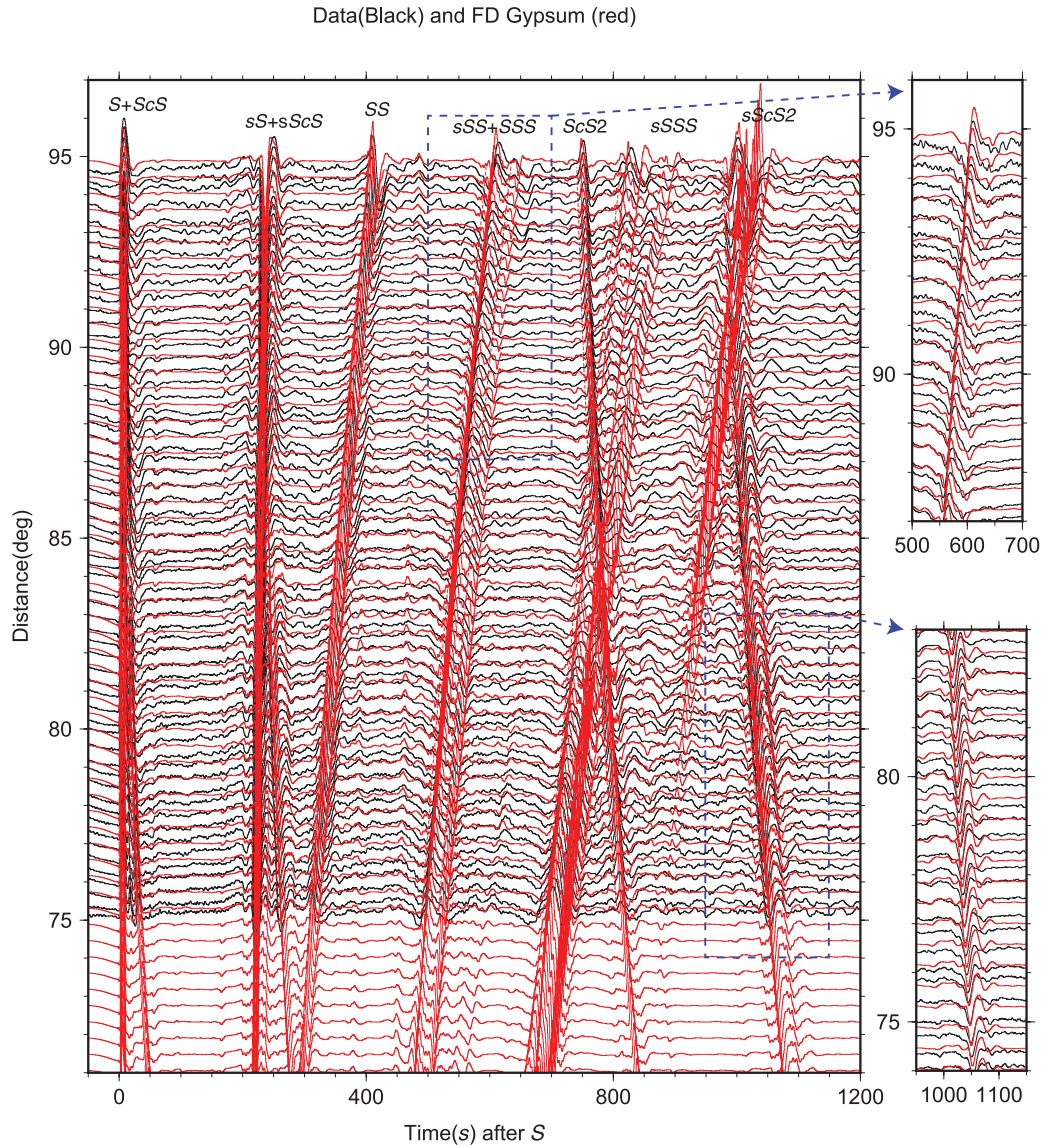


**Figure 4.** Comparison of data (black) and the finite-difference synthetics (red) for the  $SH$  displacement. Without of attenuation in the current FD code, the waveform difference is substantial especially for the late phases. To account for attenuation, we apply a  $t\ast$  of 8 s to the FD synthetics (shown in the right-hand side two subplots for  $sSS$  and  $sScS2$  phases), and obtain better fits with the data.

Therefore, if we generate the line source seismograms  $V_{2D}(x, z, t)$  along a horizontal profile, we can process adjacent traces using eq. (7) to obtain  $p(t)V_{2D}(x, z, t)$ . Next, by taking the square root of the product of  $V_{2D}(x, z, t)$  and  $p(t)V_{2D}(x, z, t)$ , and paying attention to the sign, we obtain

$$\sqrt{p(t)V_{2D}(x, z, t)} = \text{sgn}(V_{2D})\sqrt{|V_{2D} \times p(t)V_{2D}|}. \quad (9)$$

By convolving with the remaining part in eq. (3), we can then obtain the point source seismogram at a particular receiver. This procedure works very well when comparing results with other methods as demonstrated in this paper later.

## 2.2 Moment tensor source

In 2-D simulation, we can simulate only line sources. We show that by correcting the 3-D spreading, we can transfer line source seismograms to point source seismograms. Now we will discuss how a point dislocation source (an earthquake with 3-D radiation

pattern) is handled in 2-D FD code. The first method uses the moment tensor approach, which the 3-D case is discussed in detail in Graves (1996).

Note that, in global modelling, receivers are distributed at different azimuths. The azimuth variation is thus due to both variation of material properties and earthquake radiation pattern. The former one can only be accounted for by conducting 2-D simulation at each azimuth of interest. Such kind of scaling of computing cost with the number of azimuth is inevitable. However, in the azimuth bins of interest, if we assume material properties do not change with azimuth, then the azimuth variation is purely due to earthquake radiation pattern. This kind of azimuth variation is equivalent to the case where receivers are at one azimuth but earthquake itself changes its strike. Since earthquake moment tensor is combination of several elementary tensors, then by combination of synthetics for these elementary moment tensor, we can account for azimuth variation in the latter case at no extra simulations.

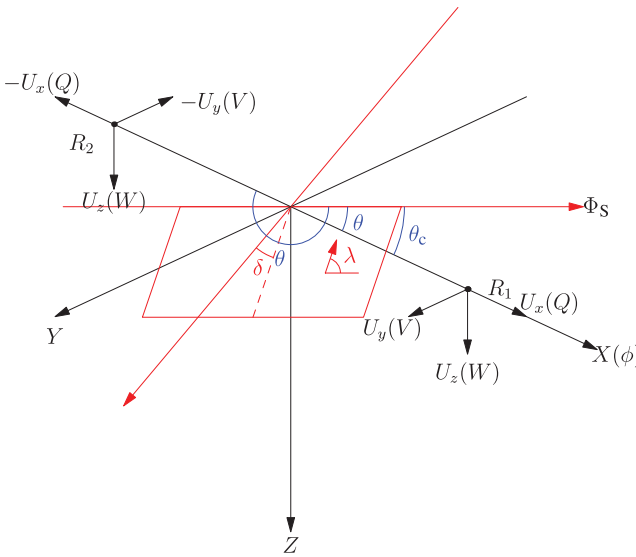


**Figure 5.** Coordinates systems. The dislocation source is at the origin, with the following fault parameters: strike  $\Phi_s$ , rake  $\lambda$ , dip  $\delta$ . The receiver  $R_1$  is at azimuth  $\phi$ ,  $R_2$  is at azimuth  $\phi + \pi$ . In cylindrical coordinate  $(\theta, r, z)$ ,  $\theta$  is the clockwise angle from the strike to the receiver. The direction for  $SH$  displacement ( $V$ ) and  $P-SV$  displacement ( $Q$  and  $W$ ) is also shown. In Cartesian coordinate,  $X$  points to the receiver direction,  $Z$  points downwards. The displacement for  $P-SV$  is  $(U_x, U_z)$ , for  $SH$  is  $U_y$ . Define  $\theta_c = \phi - \Phi_s$ , the clockwise angle from strike ( $\Phi_s$ ) to positive  $X$ -direction ( $\phi$ ). In the FD source injection, we need to know the displacement in a box surrounding the point dislocation. Note that for the  $x \geq 0$  region,  $r = x$ ,  $\theta = \theta_c$ ,  $U_x = Q$ ,  $U_y = V$ ,  $U_z = W$ ; and for the  $x < 0$  region,  $r = -x$ ,  $\theta = \theta_c + \pi$ ,  $U_x = -Q$ ,  $U_y = -V$ ,  $U_z = -W$ .

In Cartesian coordinates shown in Fig. 5, the earthquake source is at the origin,  $Z$  points downwards and  $X$  points to receiver azimuth  $\phi$ . All material properties are assumed invariant in  $Y$ -direction. For a double-couple source (strike  $\phi_s$ , rake  $\lambda$ , dip  $\delta$ ), the elementary moment components are (Aki & Richards 1980)

$$\begin{aligned} M_{xx} &= -(\sin \delta \cos \lambda \sin 2\Phi + \sin 2\delta \sin \lambda \sin^2 \Phi), \\ M_{xy} &= \sin \delta \cos \lambda \cos 2\Phi + 1/2 \sin 2\delta \sin \lambda \sin 2\Phi, \\ M_{xz} &= -(\cos \delta \cos \lambda \cos \Phi + \cos 2\delta \sin \lambda \sin \Phi), \\ M_{yy} &= \sin \delta \cos \lambda \sin 2\Phi - \sin 2\delta \sin \lambda \cos^2 \Phi, \\ M_{yz} &= -(\cos \delta \cos \lambda \sin \Phi - \cos 2\delta \sin \lambda \cos \Phi), \\ M_{zz} &= \sin 2\delta \sin \lambda, \end{aligned} \quad (10)$$

where  $\Phi = \Phi_s - \phi$  is the effective strike in this coordinate system.

In 2-D simulation, we cannot simulate all six components, but fortunately we do not need to. The far-field radiation for  $P-SV$  and  $SH$  is after Chapman (2004, p. 123)

$$\begin{aligned} P(M; \phi_1, \phi_2) &= (M_{xx} \cos^2 \phi_1 + M_{yy} \sin^2 \phi_1 + M_{xy} \sin 2\phi_1) \sin^2 \phi_2 \\ &\quad + M_{zz} \cos^2 \phi_2 + (M_{zx} \cos \phi_1 + M_{yz} \sin \phi_1) \sin 2\phi_2, \\ SV(M; \phi_1, \phi_2) &= 1/2 (M_{xx} \cos^2 \phi_1 + M_{yy} \sin^2 \phi_1 - M_{zz} \\ &\quad + M_{xy} \sin 2\phi_1) \sin 2\phi_2 \\ &\quad + (M_{zx} \cos \phi_1 + M_{yz} \sin \phi_1) \cos 2\phi_2, \\ SH(M; \phi_1, \phi_2) &= [1/2(M_{yy} - M_{xx}) \sin 2\phi_1 + M_{xy} \cos 2\phi_1] \sin \phi_2 \\ &\quad + (M_{yz} \cos \phi_1 - M_{zx} \sin \phi_1) \cos \phi_2. \end{aligned} \quad (11)$$

Here  $\phi_1$ , and  $\phi_2$  are the spherical coordinate azimuth angle and inclination angle, respectively. Thus, in the  $XZ$ -plane we choose

$\phi_1 = 0$ , then

$$\begin{aligned} P(M; \phi_2) &= M_{xx} \sin^2 \phi_2 + M_{zz} \cos^2 \phi_2 + M_{zx} \sin 2\phi_2, \\ SV(M; \phi_2) &= 1/2 (M_{xx} - M_{zz}) \sin 2\phi_2 + M_{zx} \cos 2\phi_2, \\ SH(M; \phi_2) &= M_{xy} \sin \phi_2 + M_{yz} \cos \phi_2. \end{aligned} \quad (12)$$

So only  $M_{xx}$ ,  $M_{zz}$ ,  $M_{xz}$  contribute to the far-field  $PSV$  system in the  $XZ$ -plane, and only  $M_{xy}$ ,  $M_{yz}$  contribute to the far-field  $SH$  system in the  $XZ$ -plane. And for these components, we can interface them in 2-D FD code.

We followed the approach of Coutant *et al.* (1995) to insert the moment tensors into the 2-D FD code via the velocity–stress formulation of elastodynamics equation

$$\begin{aligned} \rho \frac{\partial \dot{u}_i}{\partial t} &= T_{ij,j}, \\ \frac{\partial T_{ij}}{\partial t} &= c_{ijkl} \dot{u}_{k,l} - m_{ij}, \end{aligned} \quad (13)$$

where  $\dot{u}_i$  is the velocity,  $T_{ij}$  the stress, subscript  $,j$  differentiation,  $c_{ijkl}$  the elastic parameter and  $m_{ij}$  seismic moment density. For a point dislocation source  $m_{ij} = M_{ij} f(t) \delta(\mathbf{x} - \mathbf{x}_s)$ , where  $f(t)$  is the seismic source-time function,  $\mathbf{x}$  is 2-D spatial coordinate, and  $\mathbf{x}_s$  is the source location. In the FD simulation,  $\delta(\mathbf{x} - \mathbf{x}_s)$  is replaced by  $1/(\Delta h)^2$ , an average over the grid cell, where  $\Delta h$  is the FD grid size. Then at every time step, the source injection is done by updating the stress components at the source gridpoints

$$T_{ij} \leftarrow T_{ij} - \Delta t M_{ij} \dot{f}(t) / (\Delta h)^2. \quad (14)$$

### 2.3 Transparent source box

The momentum approach is simple and compact in space. However, a classic approach discussed in this section has the advantage of modelling some complex sources.

Here, we follow the transparent box approach used by Alterman & Karal (1968) and Vidale *et al.* (1985) to add the source into the FD. This procedure becomes more complicated in staggered-grid FD. The basic idea is to divide the elastic wavefield  $A$  into two parts, one of which is the known analytical source part  $S$ , and the other is the unknown part  $R$  that accounts for interactions with the structure, so  $A = S + R$ . Conceptually, we will conduct two FD simulations. One is within the source region and only updates  $R$ , the other is outside the source box and updates  $A$ . The two simulations exchange information through the boundary.

In Fig. 6, the FD grids are divided into four parts, where part (1)(2) is the region where we update  $A$ , and part (3)(4) is the region where we update  $R$ . In the first FD simulation that updates  $A$ , we need to know  $A$  at part (3) as a boundary condition. In part (3), we only know  $R$  from the second FD simulation at previous time step, but we can use  $A = R + S$  to obtain  $A$  at region (3), provided that we can calculate  $S$  analytically. Similarly, in the second FD simulation that updates  $R$ , we need  $R$  in part (2) as a boundary condition. We only know  $A$  in part (2) from the first simulation at previous time step, but we can obtain  $R$  from  $R = A - S$ .

In detail, for either  $PSV$  or  $SH$  system, one FD step for updating stress  $T$  and velocity  $V$  requires:

- (1)  $V_A^n = V_R^n + V_S^n$  in region (3),
- (2)  $(T_A^{n-1/2}, V_A^n) \rightarrow T_A^{n+1/2}$  in regions (1) and (2),
- (3)  $V_R^n = V_A^n - V_S^n$  in region (2),
- (4)  $(T_R^{n-1/2}, V_R^n) \rightarrow T_R^{n+1/2}$  in regions (3) and (4),
- (5)  $T_A^{n+1/2} = T_R^{n+1/2} + T_S^{n+1/2}$  in region (3),
- (6)  $(V_A^n, T_A^{n+1/2}) \rightarrow V_A^{n+1}$  in regions (1) and (2),

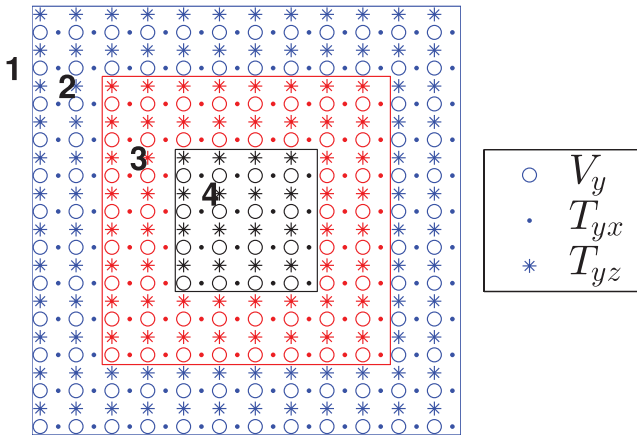


**Figure 6.** The source box for a staggered-grid finite difference for the  $SH$  case. Part (1)(2) is the region for updating  $A$ . Part (2)(3) is the region for updating  $R$ . We need to compute source wavefield  $S$  analytically at part (2)(3). Note that as a boundary condition for simulation of  $R$  in (3), the width of part (2) should be larger enough to accommodate the width of FD stencil centred on part (3). Similarly, width of part (3) should be larger enough to accommodate the width of FD stencil centered on part (2). Here, the finite difference stencil width is four gridpoints (two points on each side), so we choose width of regions (2) and (3) to be two gridpoints. There are no limit on how large part (4) can be, as long as it is large enough to accommodate the width of FD stencil in part (3).

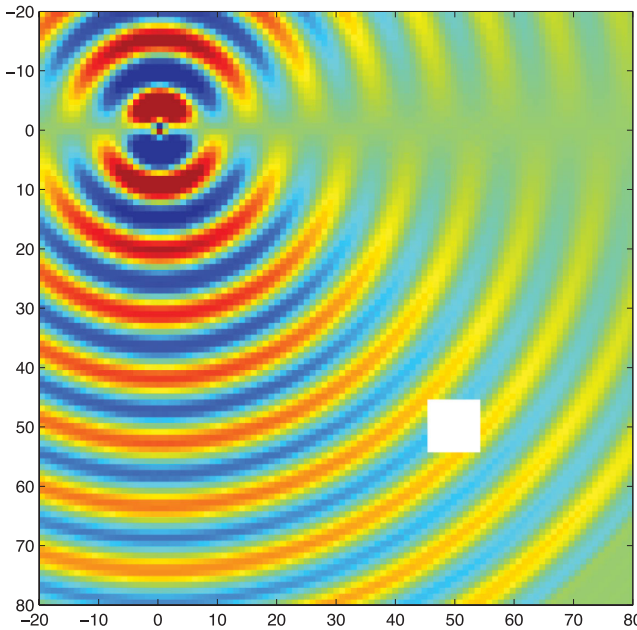


**Figure 7.** The wavefields radiated from a monotone source outside of the box (white region). Although no explicit updating of the total wavefield inside the box, the wavefield passes the box smoothly as if it does not exists.

$$(7) \quad T_R^{n+1/2} = T_A^{n+1/2} - T_S^{n+1/2} \text{ in region (2),}$$

$$(8) \quad (V_R^n, T_R^{n+1/2}) \rightarrow V_R^{n+1} \text{ in regions (3) and (4).}$$

This approach allows the scattered wavefields to pass the source box as if the box does not exist, which is termed ‘transparent source box’ (Aki & Richards 1980), see Fig. 7.

Vidale *et al.* (1985) and Helmberger & Vidale (1988) proposed an approach widely used to interface the 2-D FD method with Cagniard-de Hoop source description that accounts for the 3-D earthquake radiation pattern. However, their approach produces a

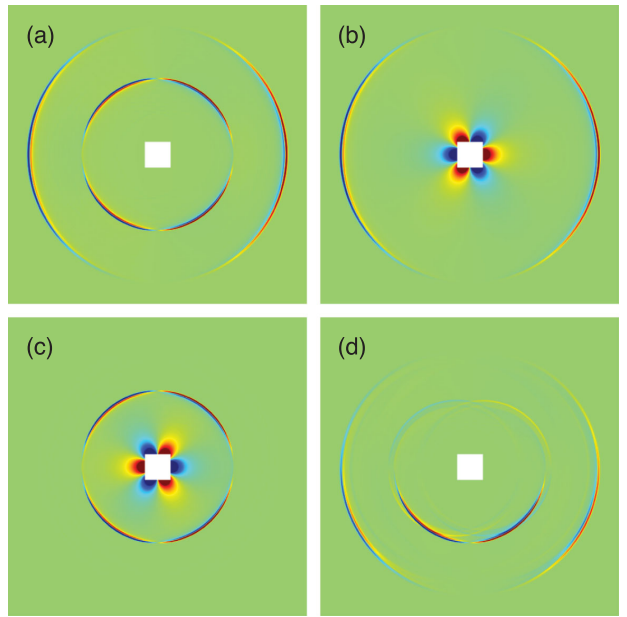


**Figure 8.** Demonstration of box sources for (a) a dislocation source; (b) its  $P$ -wave component; (c) its  $S$ -wave component and (d) its downgoing component. The white box is the source region. Note the  $P$  and  $S$  components separately are unstable, but their sum (a) is stable.

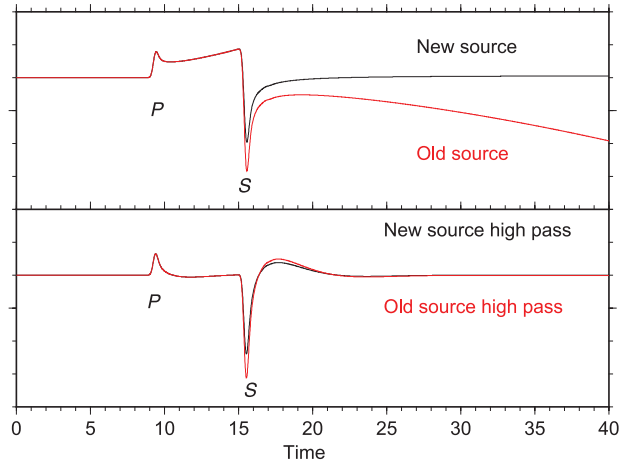


**Figure 9.** The old source box has the low-frequency late-time drift and can be mitigated using a high-pass filter. The new source box does not have the drift. Note that the  $S$  phase amplitude of the old source is bigger because of an extra  $\sqrt{\alpha/\beta}$  factor compared with that of the new source.

late-time drift, which obscures late arrivals like surface waves. To understand the cause of drift, we take a point dislocation source (pure strike-slip) in homogeneous media as an example. In their approach, using cylindrical coordinates (Fig. 5), the vertical displacement at position  $(\theta, r, z)$  in homogeneous media will be (see Appendix for details)

$$W = W_\alpha + W_\beta, \quad (15)$$

where  $\alpha, \beta$  denote the  $P$  and  $S$  contribution, respectively. In detail

$$\begin{aligned} W_\alpha &= \frac{M_0}{4\pi\rho} \frac{2}{\pi} A(\theta, \lambda, \delta) \frac{d}{dt} \left\{ \frac{1}{\sqrt{2r}} \frac{1}{\sqrt{t}} * \text{Im} \left[ (-p^2) \frac{\sqrt{p}}{\eta_\alpha} (-\varepsilon \eta_\alpha) \frac{dp}{dt} \right] \right\}, \\ W_\beta &= \frac{M_0}{4\pi\rho} \frac{2}{\pi} A(\theta, \lambda, \delta) \frac{d}{dt} \left\{ \frac{1}{\sqrt{2r}} \frac{1}{\sqrt{t}} * \text{Im} \left[ (-\varepsilon p \eta_\beta) \frac{\sqrt{p}}{\eta_\beta} (p) \frac{dp}{dt} \right] \right\}, \end{aligned} \quad (16)$$

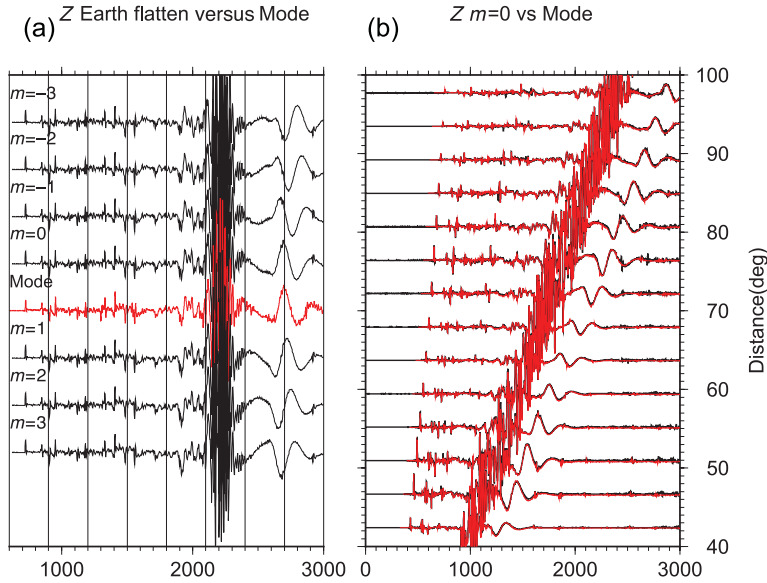


**Figure 10.** (a) Comparison of vertical displacement seismograms at  $90^\circ$  for the PREM using different  $m$  with mode summation synthetics. It appears that  $m = 0$  best fits the fundamental Rayleigh around 2700 s in these cases. (b)  $m = 0$  synthetics (red) fits mode summation Rayleigh wave (black) at other distances as well.

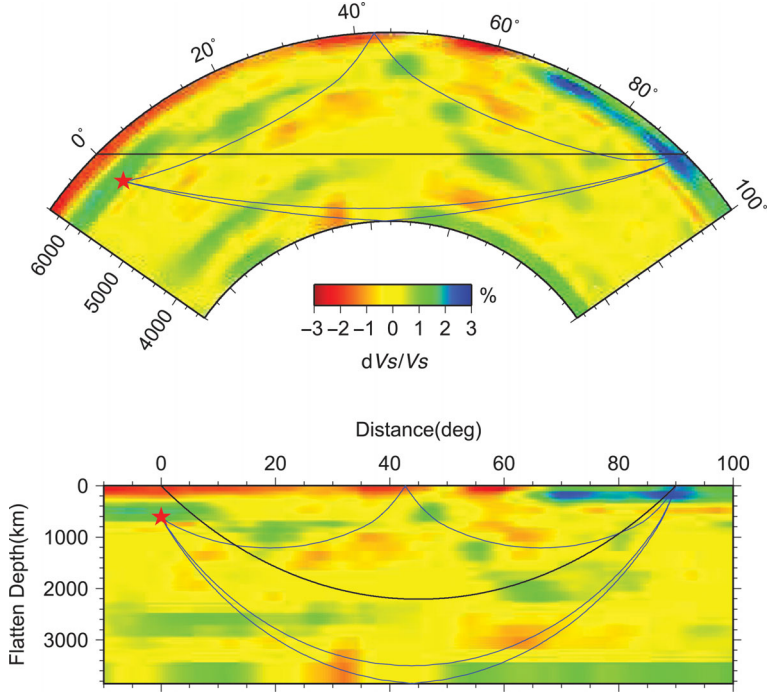


**Figure 11.** The tomography model in the spherical Earth (upper panel) and its earth flattened version (lower panel). The ray paths for  $S$ ,  $ScS$  and  $SS$  are shown as blue lines. The black line indicates the geometric ray path for a homogeneous whole space.

where  $M_0$  is the seismic moment,  $\rho$  is the density,  $r$  is the horizontal distance between source and receiver,  $\varepsilon$  is the sign of Z-coordinate of the receiver,  $A(\theta, \lambda, \delta)$  is a function depending on earthquake focal mechanism (strike assumed at 0, rake  $\lambda$ , dip  $\delta$ ) and azimuth of the receiver  $\theta$  and

$$p = \frac{r}{R^2} t + i \left( t^2 - \frac{R^2}{v^2} \right)^{1/2} \frac{|z|}{R^2},$$

$$\eta_v = \frac{|z|}{R^2} t - i \left( t^2 - \frac{R^2}{v^2} \right)^{1/2} \frac{r}{R^2}, \quad v = \alpha, \beta \quad (17)$$

with  $i = \sqrt{-1}$ .

Because of the singularity at  $t = R/v$  for the term

$$\frac{1}{\eta} \frac{dp}{dt} = \frac{i}{(t^2 - R^2/v^2)^{1/2}}, \quad (18)$$

the most contribute comes from the time when phase first arrives. Eq. (17) then becomes  $p \approx r/Rv = p_0$ , thus the term in eq. (16) can be simplified

$$\text{Im} \left[ \sqrt{p} (\dots) \frac{1}{\eta} \frac{dp}{dt} \right] \approx \text{Im} \left[ \sqrt{p_0} (\dots) \frac{1}{\eta} \frac{dp}{dt} \right]$$

$$= \sqrt{p_0} \text{Im} \left[ (\dots) \frac{1}{\eta} \frac{dp}{dt} \right] = \sqrt{p_0(t)} W_{2D}. \quad (19)$$

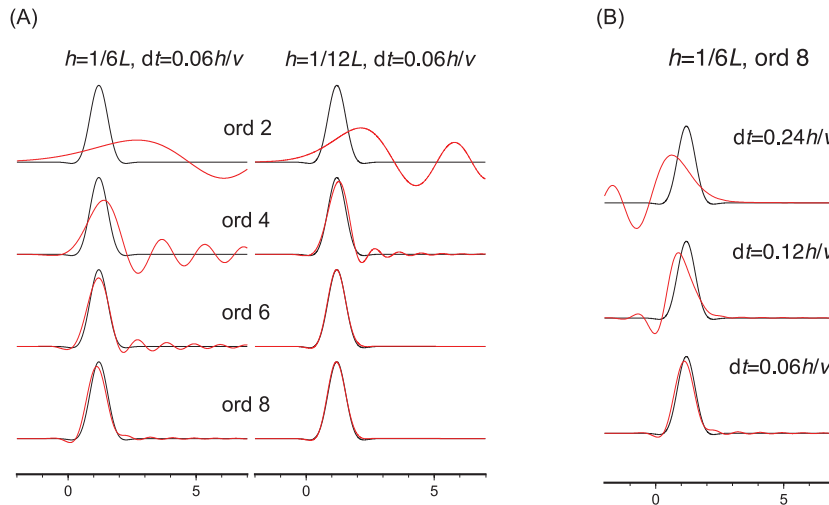


**Figure 12.** Illustration of dispersion error assuming  $SH$  simulation in a homogeneous space. The  $S$  velocity  $v$  is  $6 \text{ km s}^{-1}$ , and the source-time function is of Gaussian shape with central frequency 1 Hz, which gives a wavelength  $L$  of 6 km. The source-receiver distance is 6000 km, which is  $1000L$ . (a) Demonstration of spatial dispersion. Red traces are simulation results, and black is the analytical calculation. For two cases of grid space of  $h = 1/6L$  and  $h = 1/12L$ , dispersion error reduces as we increase spatial discretization order. The time discretization is very fine and its dispersion error can be neglected. (b) Demonstration of temporal dispersion. For  $h = 1/6L$  and eighth-order spatial discretization, time dispersion error decreases as we reduce the time step.

Then it can be verified that the  $W_{2\text{D}}$  part is indeed a line source solution and satisfies the 2-D wave equation. Thus, it can be interfaced with 2-D FD to propagate to further distance from the source. Note  $p_0$  (the geometric ray parameter) is the same as  $p$  in eq. (3).

The above  $W_{2\text{D}} = W_{2\text{D},\alpha} + W_{2\text{D},\beta}$  consists of the  $P$  and  $S$  part respectively. It can be shown that  $W_{2\text{D},\alpha}$  and  $W_{2\text{D},\beta}$  each individually goes into infinity as  $t \rightarrow \infty$ , but their summation  $W_{2\text{D}}$  does not. For example, wavefield snapshots of  $W_{2\text{D}}$ ,  $W_{2\text{D},\alpha}$  and  $W_{2\text{D},\beta}$  generated using the ‘transparent box approach’ are shown in Figs 8(a), (b) and (c), respectively. Note the drift terms appear around source box in Figs 8(b) and (c), but they are of opposite sign and are cancelled as shown in Fig. 8(a).

In Vidale & Helmberger (1987), however, the authors approximated  $\sqrt{p_0(t)/r}$  using  $\sqrt{1/R\alpha}$  for  $W_\alpha$  part, and  $\sqrt{1/R\beta}$  for  $W_\beta$  part. They then interfaced 2-D FD with a source  $W_{2\text{D}}^* = \sqrt{1/\alpha}W_{2\text{D},\alpha} + \sqrt{1/\beta}W_{2\text{D},\beta}$ . In this way, the drifting term will not be cancelled, and  $W_{2\text{D}}^* \rightarrow \infty$  as  $t \rightarrow \infty$ . The seismograms generated using the original formulation (old source) and the new one are compared in Fig. 9. Although the drift is of low frequency and can be mitigated using a high-pass filter, it becomes large in amplitude at late-time, and contaminates the late arrivals, making it difficult to use in global modelling. The new source approach does not have this problem.

The source box approach has the advantage that it can be used to represent some complex sources. For example, in Figs 8(b) and (c), we show that we can interface with only the  $P$  part or the  $S$  part of the wavefield. Note that, the  $P$  and  $S$  parts each separately has the correct radiation pattern, which is hard to obtain using the moment tensor approach. We can also simulate only the downgoing wavefield by nullifying the wavefield in the upper half of the source box, as shown in Fig. 8(d). Although the separation of downgoing part is not perfect, such flexibility proves useful in some studies, such as studies involving directivity (Saikia & Helmberger 1997), and the identification of depth phases.

While the above 2-D approaches are equivalent to an asymptotic double-couple solution, the so-called far-field solution, thus may

break down at very long periods, it proves useful as demonstrated below.

#### 2.4 Earth-flattening transform

Since global models are sensitive to the Earth’s curvature, in Cartesian coordinate simulation, the treatment of Earth flattening becomes essential. A particularly simple transformation was proposed by Müller (1971),

$$\begin{aligned} z &= a \log \frac{a}{r}, \\ \alpha_f &= \alpha_s \frac{a}{r} \\ \beta_f &= \beta_s \frac{a}{r}, \end{aligned} \quad (20)$$

where  $z, \alpha_f, \beta_f$  are the depth, and velocities in the flat model,  $r, \alpha_s, \beta_s$  are the radius and velocities in the spherical model and  $a$  is the radius of the Earth. This Earth-flattening transform gives the correct kinetics of wave propagation for a layered Earth. To obtain the correct amplitude, we also need a transform for density, which usually take the following form

$$\rho_f(z) = \rho_s \left( \frac{r}{a} \right)^{m+2}, \quad (21)$$

where  $m$  is to be determined.

For an  $SH$  system in layered media, Biswas & Knopoff (1970) shows that an exact Earth-flattening transformation is achieved by setting  $m = 3$ . However, an exact Earth flattening transformation does not exist for the  $P$ - $SV$  system, and  $m$  from  $-3$  to  $3$  have been considered (Chapman 1973). An  $m = -3$  appears to be optimal in a layered fluid, which has the same transformation of density as that used for velocities (Helmberger 1973). Another commonly used value is  $m = -2$ , which keeps  $\rho_f(z) = \rho_s(r)$  (Müller 1971).

Given the same seismic moment in Cartesian code, the absolute amplitude of the body wave increases as  $m$  increases (which means a decrease in  $\rho_f$ ). Our numerical tests show that, at distance of  $90^\circ$ ,

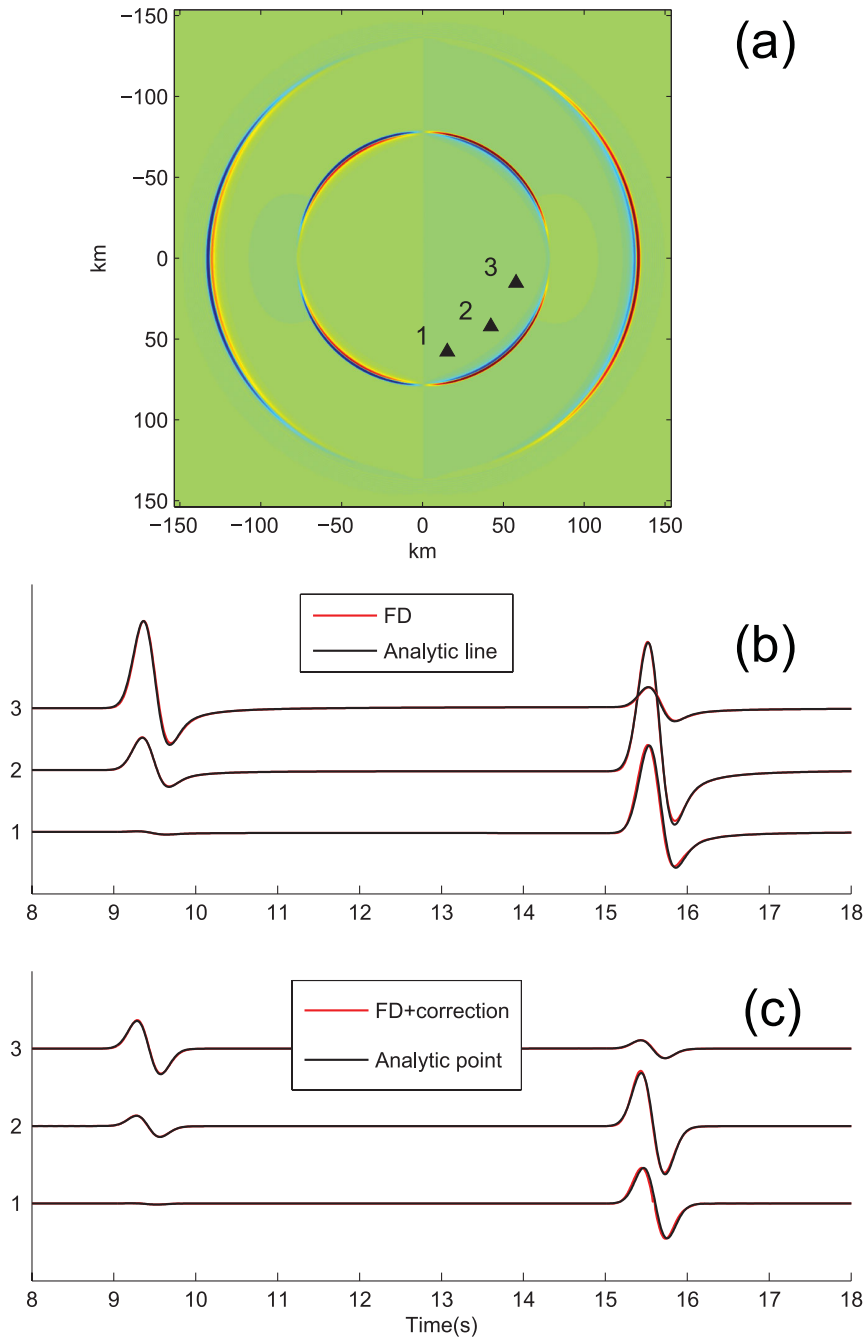


**Figure 13.** Comparison of FD synthetics with the analytic solution. (a) The source is at the origin. Three receivers are shown as black triangle. The snapshot shows the radial component wavefield from a strike-slip fault. (b) Comparison of the line source velocity seismogram generated by FD and by analytical calculations at the three receivers. (c) Comparison of point source velocity seismogram obtained from post-processing the line source FD simulation and from analytical calculation.

a unit increase of  $m$  value results in an increase of 5 per cent in the  $P$ -wave amplitude. However, as shown in Fig. 10(a), the relative amplitude and waveform complexity of body wave changes little as we change  $m$ , and the largest differences between the results are in the fundamental Rayleigh wave phase. The fundamental Rayleigh wave has a very long period and is sensitive to Earth's curvature and density (Dahlen & Tromp 1998). A searching for appropriate  $m$  value shows that  $m = 0$  fits the Rayleigh wave better than other integer  $m$ , although at these periods self-gravitation, the Earth's rotation become important issues, and because these are already embedded in the SEM, it is the preferred method at these periods.

As discussed in Gilbert & Helmberger (1972), transferring the synthetics from flattened earth model to spherical earth model needs another amplitude correction

$$U^{(s)} \approx \sqrt{\Delta / \sin \Delta} U^{(f)}, \quad (22)$$

where  $\Delta$  is the epicentral distance in degrees.

The above Earth-flattening transform is for a 1-D spherical Earth. For a lateral varying tomographic model, we apply Earth-flattening transform to each vertical profile, as in many previous studies. A demonstration of the transformation with several ray paths is shown in Fig. 11, see Helmberger (1973) for details.

## 2.5 FD implementation

FD methods in seismology have been discussed by many authors. In our implementation, we use the staggered-grid velocity–stress scheme (Virieux 1984; Levander 1988), which can account for solid–fluid interface automatically. For the *SH* system, the free surface is implemented using stress imaging method; for *P-SV* system, we use the method in Mittet (2002). For absorbing boundary condition, we use the parameter in Zhang & Shen (2010). The code is written using CUDA (Micikevicius 2009) and parallelized using pthread on three GPUs within one computing node, which for our 2-D case having a speedup around 100 compared with a single CPU.

To reduce spatial dispersion caused by discretization, we use eighth-order central difference in space. Second-order central difference is used for time discretization in staggered-grid method, whose dispersion error can be mitigated by reducing the time step, which does not increase simulation memory requirements. Detailed analysis of this scheme is discussed in Virieux (1984) and Levander (1988). Here, we show an example to illustrate the dispersion error. In a homogeneous space with *S* velocity of  $6 \text{ km s}^{-1}$ , we conduct an *SH* simulation with a source-time function of Gaussian shape (central frequency about 1 Hz and wavelength 6 km). The source–receiver distance is 6000 km, which corresponding propagating 1000 cycles. In Fig. 12(a), we show how the spatial dispersion is reduced by increasing spatial discretization order or halving the grid space. In Fig. 12(b), we show how the temporal dispersion is mitigated by reducing the time step. Note the phase delay of spatial dispersion and phase advance of temporal dispersion.

**Table 1.** Layered crust model.

Thickness (km)	$v_p (\text{km s}^{-1})$	$v_s (\text{km s}^{-1})$	Density ( $\text{g cc}^{-1}$ )
3.95	4.4	2.51	2.0
10.0	6.0	3.46	2.6
16.0	6.7	3.87	2.9
$\infty$	7.7	4.5	3.3

## 3 VALIDATION

### 3.1 Regional modelling

We begin with the simplest problem, producing synthetics for a strike-slip fault in a homogeneous space, to test the radiation patterns and 2-D to 3-D correction. A snapshot of the radial velocity wavefield in the *XZ*-plane is shown in Fig. 13(a), with three receivers distributed to sample the radiation pattern. The raw FD synthetics (velocity seismogram for the line source) are shown in Fig. 13(b), along with the line source analytical results. After 3-D spreading correction, we obtain the point source seismograms in Fig. 13(c), which are in good agreement with the point source analytical results. Note the wavelet shape difference between line source seismograms and point source seismograms, and 3-D correction is necessary to recover the given wavelet shape, which is the derivative of a Gaussian source-time function in this case.

Next, we considered a layered crust (Table 1) using a double-couple source with a strike of  $201^\circ$ , a dip of  $10^\circ$  and a rake of  $90^\circ$ . The event is at a depth of 10 km. The source-time function is a triangle with a length of 0.6 s. In Fig. 14, we display the

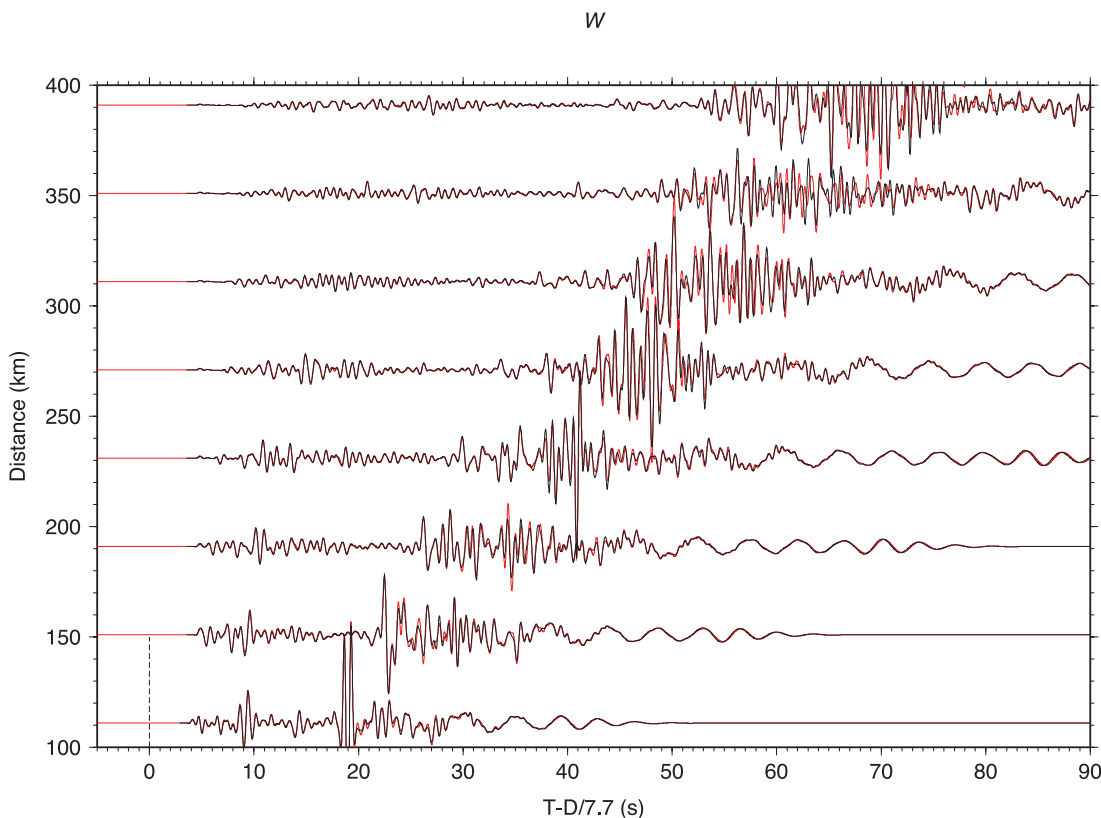


**Figure 14.** Comparison of vertical (*Z*) component seismograms generated by FD (red) and FK (black) for the layered model shown in Table 1. The source is a double couple with strike  $201^\circ$ , dip  $10^\circ$  and rake  $90^\circ$ . The receivers are at an azimuth of  $270^\circ$ . The source-time function is a symmetrical triangle with a length of 0.6 s. The FD simulation has grid size of 0.1 km and a time step of 0.005 s.

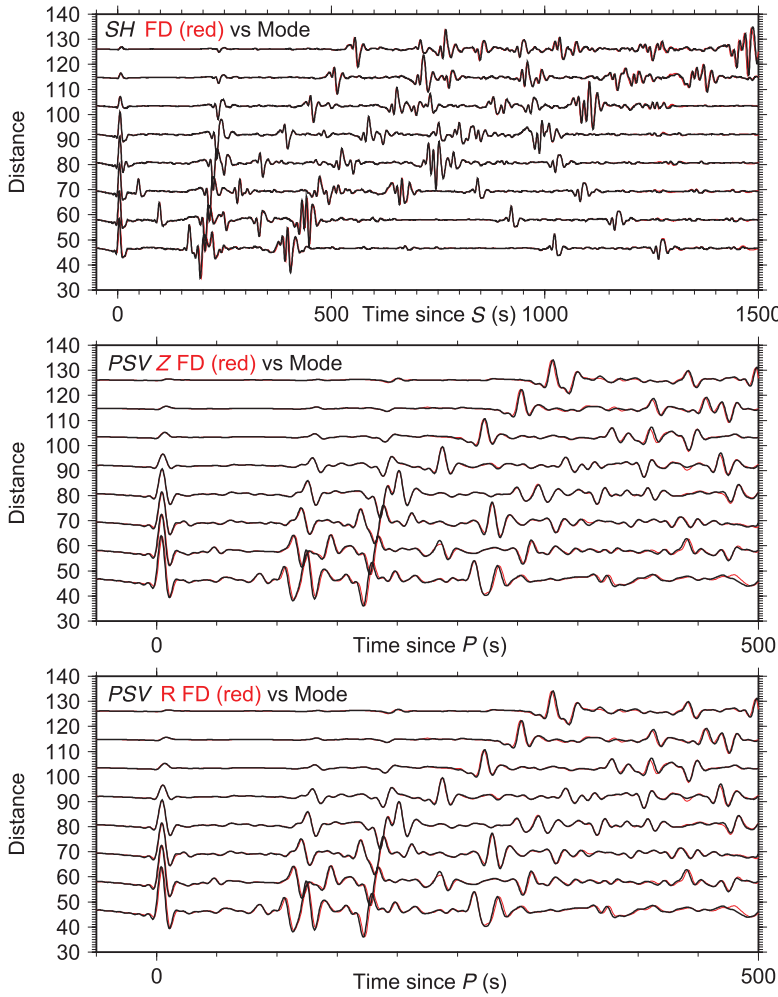


**Figure 15.** Comparison of the displacement seismograms for the PREM model generated using FD and mode summation method. The Earth-flattening transformation using  $m = 3$  for both PSV and SH system. The source is for the 2010 February 18 event, a double couple with strike  $71^\circ$ , dip  $15^\circ$  and rake  $166^\circ$ . The receivers are at an azimuth of  $37^\circ$ . The source-time function is a symmetrical triangle with a length of 10 s. The FD simulation has a grid size of 1.57 km and a time step of 0.02 s. Both synthetics are filtered to 8–100 s because mode summation is accurate for 8 s and longer.

comparison between a well-developed ‘frequency–wavenumber (FK)’ code (Zhu & Rivera 2002) and the new FD code, at an azimuth of  $270^\circ$ . The body wave parts agree well in both amplitude and phase, the surface wave agree well in the phase, but some amplitude differences exist when strong interference of multiple phases arriving at the same time, which is a limitation of our correction method.

### 3.2 Global modelling

A test of global synthetics against modes summation method for PREM model is shown in Fig. 15. Note the plots are in true amplitude, and the fit of both phase and amplitude demonstrates the effectiveness of our correction method for body wave phases. A demonstration of the effects of various 2-D to 3-D correction terms is shown in Fig. 16. After integration of the raw 2-D synthetic velocity seismogram, we obtain the displacement seismogram, which contains long-period tails associated with its line source nature. This feature is removed nicely by performing the convolution operation, which results in the point source waveform shapes. The second

step requires processing the wavefield to capture the ray parameter  $p$ , and performing the  $\sqrt{p}$  correction. Note that phases  $ScS2$ ,  $ScS3$  and  $ScS4$  have progressively smaller ray parameters, which results in different amplitude correction factors. And after making all the correction, the FD synthetics fit the FK synthetics very well.

Another benchmark for Earth flattening is shown in Fig. 17, where we compare the absolute amplitudes and their decay of  $S(Sdiff)$  and  $P(Pdiff)$  phases against mode summation method. We can see for the SH case, the fit is very good. For the P-SV case,  $m = 3$  fits the absolute amplitude of  $P(Pdiff)$  better than  $m = 0$ . Note that the relative decay for  $m = 0$  and  $m = 3$  is about the same, and both fit the mode synthetics quite well.

Finally, we compared our synthetics with 3-D SEM for a model shown in Fig. 18(a). The 2-D synthetics is generated for a cross-section displayed in Fig. 18(b). Compared with SEM, our synthetics captures most of the features in 3-D SEM synthetics as shown in Fig. 18(c). Although such demonstrations are certainly encouraging, we suggest that when 2-D models fit the data well, it is important to have the ability to check the results against other fully 3-D method.

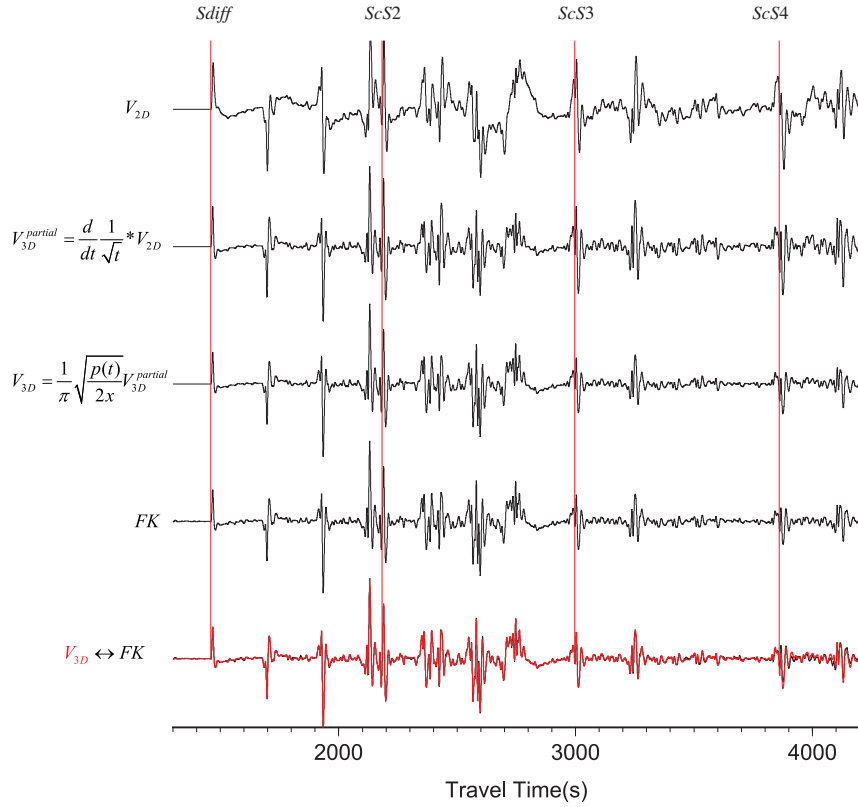


**Figure 16.** Illustration of the correction steps. The displacement  $SH$  synthetics are at a distance of  $106^\circ$ . From top to bottom, we show the 2-D finite-difference synthetics  $V_{2D}$  in displacement (an integration of raw velocity seismogram), the correction that just accounts for wavelet shape  $V_{2D}^{\text{partial}}$ , the full correction accounts for relative amplitudes of different phases  $V_{3D}$ , the FK synthetics and overlay of  $V_{3D}$  (red) with FK synthetics (black) at the bottom. All traces are high-pass filtered to 300 s and shorter period.

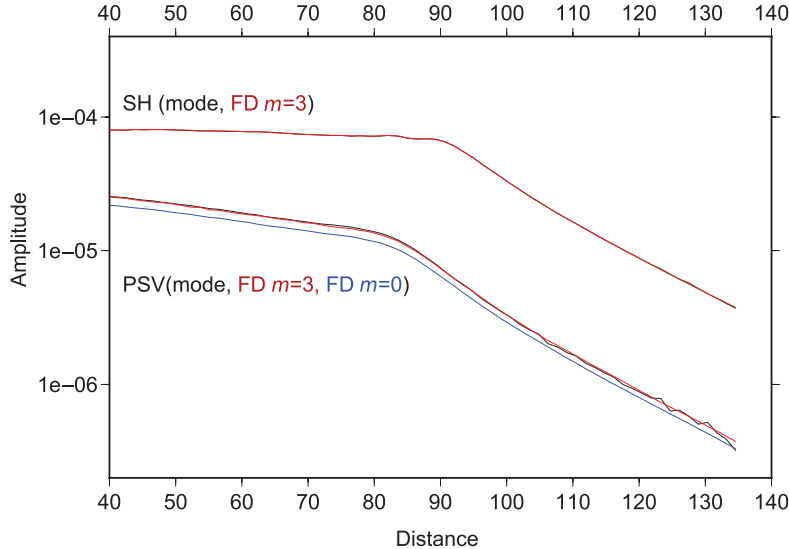


**Figure 17.** Comparison of the amplitude of synthetics between finite difference and mode summation method for  $S(S\text{diff})$  and  $P(P\text{diff})$  phases. Note in the  $P\text{-}SV$  case, the mode and FD best matches for  $m = 3$  in the Earth-flattening transformation.

#### 4 APPLICATION AND DISCUSSION

In this section, we discuss some applications of our method. Consider generating the synthetics for the data in Fig. 1. The flattened earth model is shown in Fig. 11. This cross-section along the subducted North Pacific arc is probably the most complex on Earth and was chosen here because it samples the Core Mantle Boundary

(CMB) near a known sample of a  $D'$  region (Lay & Helmberger 1983). There is a transitional structure at about  $45^\circ$  (Fig. 1) near the CMB where the wavefield begins to sample a relatively fast zone beneath North America. Because such fast zones have been associated with the  $Scd$  phases, Sidorin *et al.* (1999) suggested a mineral phase change with a positive Clapeyron slope. They also produced a global map of the phase-boundary height above the CMB,

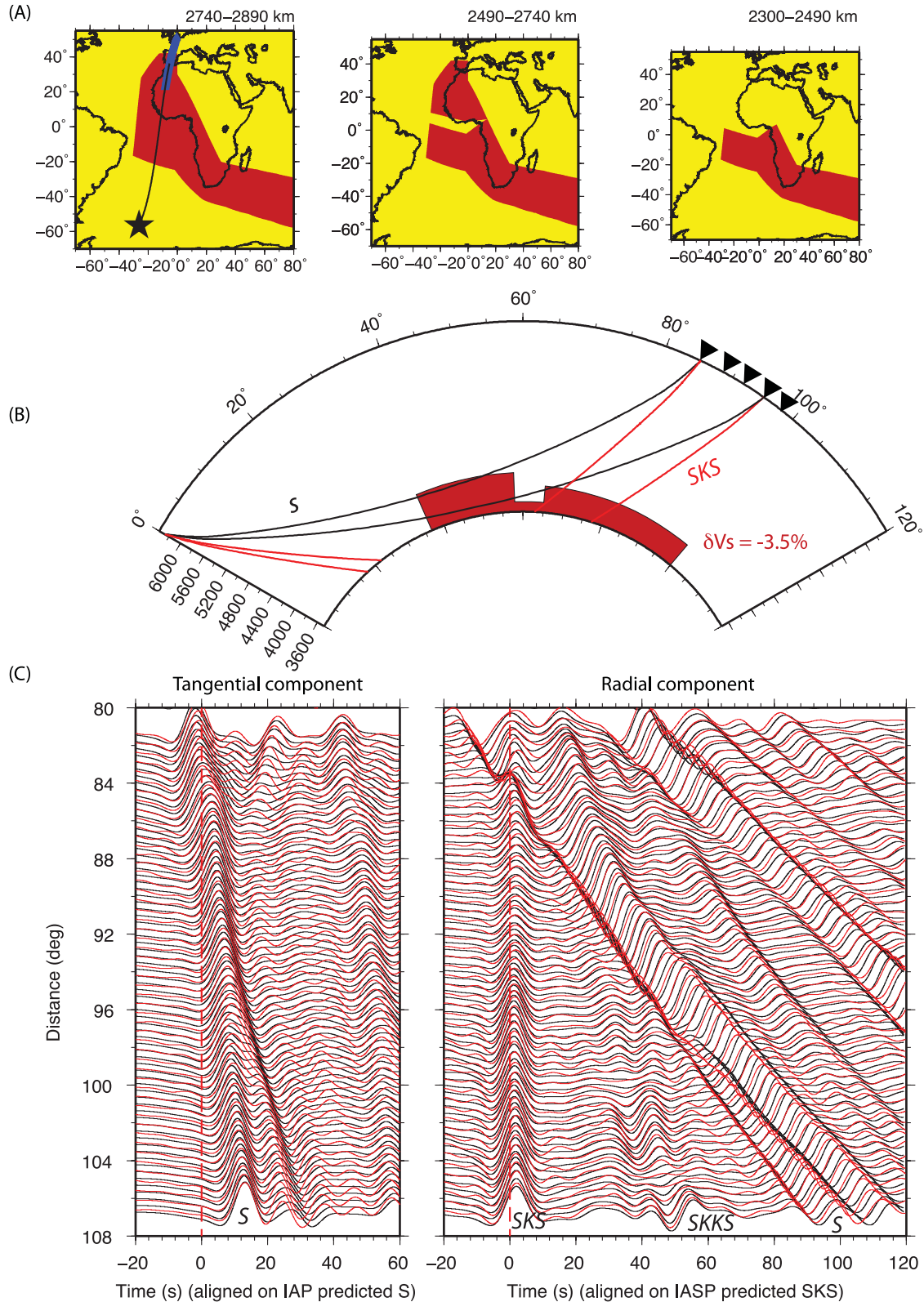


**Figure 18.** Comparison between 2-D FD and 3-D SEM synthetics. (a) The 3-D model at different depths used in the SEM calculation. The model is modified after the western edge model of the African large low shear low velocity province (Sun & Miller 2013). Here, the western edge of their model was extended further west to reduce the strong 3-D effect from the sharp edge, which makes it more suitable for 2-D calculation. The model has a uniform 3.5 per cent shear velocity reduction inside (red region). The black star shows the location of the event and blue points located at Europe denotes the dense stations along the same great circle path used in the calculation. Diagram (b) displays the 2-D cross-section along the great circle path in (a). (c) Comparison of the 2-D FD (black) and 3-D SEM (red) synthetics. The two methods produce good agreement on both traveltimes and waveforms.

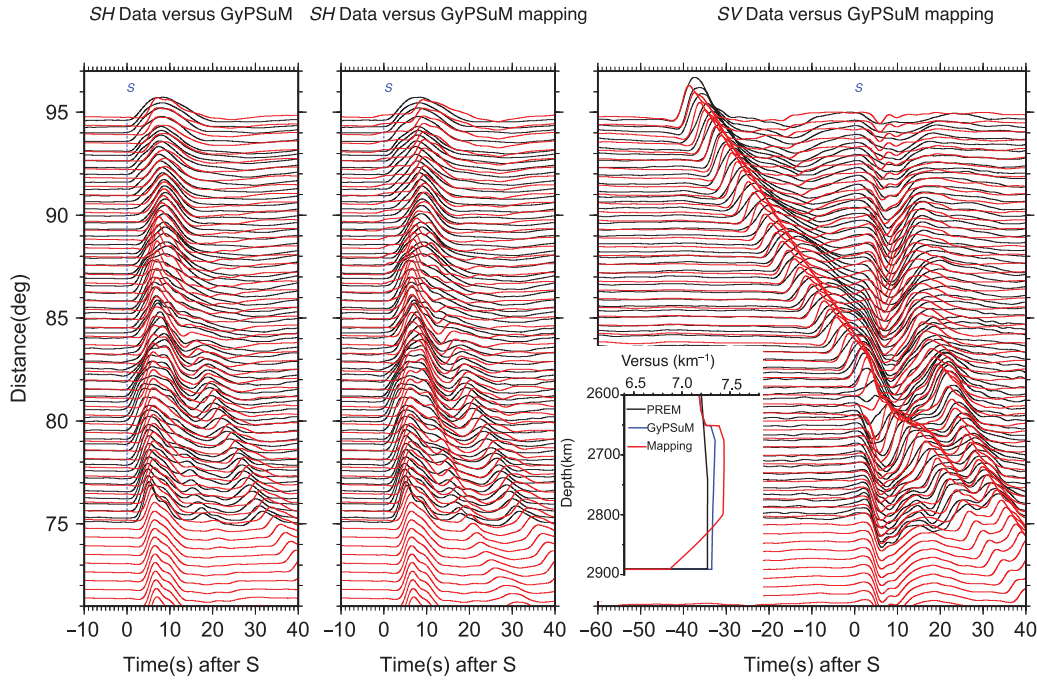


**Figure 19.** Comparison of the data (black) with FD synthetics (red) using the GyPSuM model (blue) for *SH* system is shown in (a). Comparison of the data (black) with FD synthetics (red) using the phase mapped GyPSuM model for *SH* system is shown in (b), and for *P-SV* system shown in (c).

assuming a constant shear velocity jump of 2 per cent, triggered by shear velocity tomography. An even more complicated mapping of tomographic models into a global view of the phase transition was proposed by Sun & Helmberger (2008).

To study this region, stacking of dense record sections are particularly valuable. The stack reveals the complexities of the crossing of *SKS* and *S*, as well as *SP* at the shorter distances, which are shown with GyPSuM model FD synthetics in Fig. 19(a). Although there is some success in predicting the timing shift, the apparent *Scd* phase in the *SH* section is missing, because the tomographic model does not attempt to address the phase changes directly. The phase boundary mapping prediction is included in Fig. 19(b), and fits the data much better. The fit at larger distance ( $85^\circ$ – $95^\circ$ ) is not as good as at smaller distance ( $75^\circ$ – $85^\circ$ ), where *Scd* is the second arrival. This may be due to the slab-edge effects, and such complexities can also be studied using the new FD methodology, which will be given in future efforts.

In some cases, out-of-plane model complexity (non-2-D model) is important. For example, at shorter periods, evidence of lateral variation rapidly develops. Such characteristics for Western United States have been examined in terms of multipathing by Sun & Helmberger (2011), where both in-plane and out-of-plane complexity is observed in the USAArray data for body waves. The out-of-plane features are obvious in azimuthal record sections (Sun *et al.* 2009). To model this 3-D features, we can calculate several 2-D sections using our method, and then combine them using diffraction methods. For example, a simplified approach has been presented by Helmberger & Ni (2005), where 2-D synthetics sampling the Fresnel zone region are assembled to simulate the out-of-plane features. Synthetics generated in this way match 3-D SEM results for record sections sampling the edges of the African Large Low Shear Velocity Provinces (LLSV; Ni *et al.* 2005).

Although not addressed here, there are a number of other hybrid methods that interface analytical results for a smooth varying global model with numerical results for a local complex model (Wen & Helmberger 1998). Such a method was used to model small-scale

features on the inner core–outer core boundary (Dai *et al.* 2012). We use these synthetics as another test against our code, modelling *PKiKP* phase up to 2 Hz (Li *et al.* 2014). In short, many hybrid models have been developed in this refining tomographic model approach through 2-D modelling. The resulting model can be incorporated in full 3-D SEM modelling as shown in Chen *et al.* (2007), or can be used as starting models in adjoint methods (Tape *et al.* 2009).

## 5 CONCLUSIONS

We further developed 2-D FD method for modelling the waveform complexities of relative high-frequency global seismic body waves. We have shown a new formulation of the FD source that fixes the low-frequency drift, and one that now better accounts for the 3-D spreading aspects of the wavefield. We also show that the Earth-flattening transformation is effective for global synthetics constructing, where  $m = 3$  are preferred in both the *SH* and the *P-SV* mapping. In summary, our approach, although involving many approximations, is simple and well validated against other methods, and is adequate for many applications.

## ACKNOWLEDGEMENTS

We thank the Editor and two anonymous reviewers for their comments which greatly improved the manuscript. Data were provided by the IRIS data center and EarthScope USAArray. This work was supported by NSF EAR-1053064 and CSEDI EAR-1161046 at Caltech, with partial support of D. Sun at USC under EAR-0809023.

## REFERENCES

- Aki, K. & Richards, P.G., 1980. *Quantitative Seismology: Theory and Methods*, W.H. Freeman.
- Alterman, Z. & Karal, F.C., 1968. Propagation of elastic waves in layered media by finite difference methods, *Bull. seism. Soc. Am.*, **58**(1), 367–398.

- Biswas, N. & Knopoff, L., 1970. Exact earth-flattening calculation for Love waves, *Bull. seism. Soc. Am.*, **60**(4), 1123–1137.
- Cerveny, V., 2001. *Seismic Ray Theory*, Vol. **148**, Cambridge Univ. Press.
- Chapman, C.H., 1973. The earth flattening transformation in body wave theory, *Geophys. J. R. astr. Soc.*, **35**, 55–70.
- Chapman, C.H., 2004. *Fundamentals of Seismic Wave Propagation*, Cambridge Univ. Press.
- Chen, M., Tromp, J., Helmberger, D. & Kanamori, H., 2007. Waveform modeling of the slab beneath Japan, *J. geophys. Res.*, **112**(B2), doi:10.1029/2006JB004394.
- Coutant, O., Virieux, J. & Zollo, A., 1995. Numerical source implementation in a 2D finite difference scheme for wave propagation, *Bull. seism. Soc. Am.*, **85**(5), 1507–1512.
- Crotwell, H.P., Owens, T.J. & Ritsema, J., 1999. The TauP toolkit: flexible seismic travel-time and ray-path utilities, *Seismol. Res. Lett.*, **70**, 154–160.
- Dahlen, F.A. & Tromp, J., 1998. *Theoretical Global Seismology*, Princeton Univ. Press.
- Dai, Z., Wang, W. & Wen, L., 2012. Irregular topography at the Earth's inner core boundary, *Proc. Natl. Acad. Sci. USA*, **109**(20), 7654–7658.
- Furumura, T., Kennett, B.L.N. & Furumura, M., 1998. Seismic wave field calculation for laterally heterogeneous whole earth models using the pseudospectral method, *Geophys. J. Int.*, **135**, 845–860.
- Gilbert, F. & Helmberger, D.V., 1972. Generalized ray theory for a layered sphere, *Geophys. J. Int.*, **27**(1), 57–80.
- Graves, R.W., 1996. Simulating seismic wave propagation in 3D elastic media using staggered-grid finite differences, *Bull. seism. Soc. Am.*, **86**(4), 1091–1106.
- Harkrider, D., 1964. Surface waves in multilayered elastic media. I. Rayleigh and Love waves from buried sources in a multilayered elastic half-space, *Bull. seism. Soc. Am.*, **54**(2), 627–679.
- Helmberger, D. & Harkrider, D., 1977. Modeling earthquakes with generalized ray theory, in *Modern Problems in Elastic Wave Propagation*, pp. 479–518, eds Miklowitz, J. & Achenbach, J.D., John Wiley and Sons.
- Helmberger, D.V., 1973. Numerical seismograms of long-period body waves from seventeen to forty degrees, *Bull. seism. Soc. Am.*, **63**(2), 633–646.
- Helmberger, D.V. & Ni, S., 2005. Approximate 3D body-wave synthetics for tomographic models, *Bull. seism. Soc. Am.*, **95**(1), 212–224.
- Helmberger, D.V. & Vidale, J.E., 1988. Modeling strong motions produced by earthquakes with two-dimensional numerical codes, *Bull. seism. Soc. Am.*, **78**(1), 109–121.
- Hong, T. & Helmberger, D., 1977. Generalized ray theory for dipping structure, *Bull. seism. Soc. Am.*, **67**(4), 995–1008.
- Jahnke, G., Thorne, M.S., Cochard, A. & Igel, H., 2008. Global SH-wave propagation using a parallel axisymmetric spherical finite-difference scheme: application to whole mantle scattering, *Geophys. J. Int.*, **173**(3), 815–826.
- Komatitsch, D. & Tromp, J., 1999. Introduction to the spectral element method for three-dimensional seismic wave propagation, *Geophys. J. Int.*, **139**, 806–822.
- Lay, T. & Helmberger, D.V., 1983. A shear velocity discontinuity in the lower mantle, *Geophys. Res. Lett.*, **10**(1), 63–66.
- Levander, A.R., 1988. Fourth-order finite-difference P-SV seismograms, *Geophysics*, **53**(11), 1425–1436.
- Li, D., Helmberger, D.V. & Sun, D., 2014. Notes on the variability of reflected inner-core phases, *Earthq. Sci.*, in press.
- Micikevicius, P., 2009. 3D finite difference computation on GPUs using CUDA, in *GPGPU-2: Proceedings of the 2nd Workshop on General Purpose Processing on Graphics Processing Units*, London, pp. 79–84.
- Miksat, J., Müller, T.M. & Wenzel, F., 2008. Simulating three-dimensional seismograms in 2.5-dimensional structures by combining two-dimensional finite difference modelling and ray tracing, *Geophys. J. Int.*, **174**(1), 309–315.
- Mittet, R., 2002. Free-surface boundary conditions for elastic staggered-grid modeling schemes, *Geophysics*, **67**(5), 1616–1623.
- Müller, G., 1971. Approximate treatment of elastic body waves in media with spherical symmetry, *Geophys. J. R. astr. Soc.*, **23**, 435–449.
- Ni, S.V., Helmberger, D. & Tromp, J., 2005. Three-dimensional structure of the African superplume from waveform modelling, *Geophys. J. Int.*, **161**(2), 283–294.
- Nissen-Meyer, T., Fournier, A. & Dahlen, F.A., 2007. A two-dimensional spectral-element method for computing spherical-earth seismograms—I. Moment-tensor source, *Geophys. J. Int.*, **168**(3), 1067–1092.
- Saikia, C.K. & Helmberger, D.V., 1997. Approximation of rupture directivity in regional phases using upgoing and downgoing wave fields, *Bull. seism. Soc. Am.*, **87**(4), 987–998.
- Sato, R., 1969. Formulations of solutions and for earthquake source models and some related problems, *J. Phys. Earth*, **17**(2), 101–110.
- Sidorin, I., Gurnis, M. & Helmberger, D.V., 1999. Evidence for a ubiquitous seismic discontinuity at the base of the mantle, *Science*, **286**(5443), 1326–1331.
- Simmons, N.A., Forte, A.M., Boschi, L. & Grand, S.P., 2010. GyPSuM: a joint tomographic model of mantle density and seismic wave speeds, *J. geophys. Res.*, **115**(B12), 1–24.
- Sun, D. & Helmberger, D., 2008. Lower mantle tomography and phase change mapping, *J. geophys. Res.*, **113**(B10), B10305, doi:10.1029/2007JB005289.
- Sun, D. & Helmberger, D., 2011. Upper-mantle structures beneath USArray derived from waveform complexity, *Geophys. J. Int.*, **184**(1), 416–438.
- Sun, D. & Miller, M.S., 2013. Study of the western edge of the African large low shear velocity province, *Geochem. Geophys. Geosyst.*, **14**, 3109–3125.
- Sun, D., Helmberger, D., Ni, S. & Bower, D., 2009. Direct measures of lateral velocity variation in the deep Earth, *J. geophys. Res.*, **114**, B05303, doi:10.1029/2008JB005873.
- Tape, C., Liu, Q., Maggi, A. & Tromp, J., 2009. Adjoint tomography of the southern California crust, *Science*, **325**(5943), 988–992.
- Toyokuni, G. & Takenaka, H., 2006. FDM computation of seismic wavefield for an axisymmetric Earth with a moment tensor point source, *Earth Planets Space*, **58**, 29–32.
- Tromp, J. et al., 2010. Near real-time simulations of global CMT earthquakes, *Geophys. J. Int.*, **183**(1), 381–389.
- Vidale, J.E. & Helmberger, D.V., 1987. Path effects in strong motion seismology, in *Seismic Strong Motion Synthetics*, pp. 267–320, ed. Bolt, B.A., Academic Press.
- Vidale, J.E., Helmberger, D.V. & Clayton, R.W., 1985. Finite-difference seismograms for SH waves, *Bull. seism. Soc. Am.*, **75**(6), 1765–1782.
- Virieux, J., 1984. SH-wave propagation in heterogeneous media: velocity-stress finite-difference method, *Geophysics*, **49**(11), 1933–1957.
- Wang, Y., Takenaka, H. & Furumura, T., 2001. Modelling seismic wave propagation in a two-dimensional cylindrical whole-earth model using the pseudospectral method, *Geophys. J. Int.*, **145**(3), 689–708.
- Wen, L. & Helmberger, D.V., 1998. A two-dimensional P-SV hybrid method and its application to modeling localized structures near the core-mantle boundary, *J. geophys. Res.*, **103**(B8), 17 901–17 918.
- Zhang, W. & Shen, Y., 2010. Unsplit complex frequency-shifted PML implementation using auxiliary differential equations for seismic wave modeling, *Geophysics*, **75**(4), T141–T154.
- Zhu, L. & Rivera, L.A., 2002. A note on the dynamic and static displacements from a point source in multilayered media, *Geophys. J. Int.*, **148**, 619–627.

into vertical and horizontal dependencies. A convenient form of these solutions, in terms of the Laplace-transformed displacement in the vertical ( $W$ ), tangential ( $V$ ) and radial ( $Q$ ) directions (see Fig. 5), is (Helmberger & Vidale 1988)

$$\begin{aligned}\hat{W} &= \frac{\partial \hat{\phi}}{\partial z} + sp\hat{\Omega}, \\ \hat{V} &= \frac{1}{r} \frac{\partial \hat{\phi}}{\partial \theta} - \frac{1}{spr} \frac{\partial \hat{\Omega}}{\partial z \partial \theta} - \frac{\partial \hat{\chi}}{\partial r}, \\ \hat{Q} &= \frac{\partial \hat{\phi}}{\partial r} - \frac{1}{sp} \frac{\partial \hat{\Omega}}{\partial r \partial z} + \frac{1}{r} \frac{\partial \hat{\chi}}{\partial \theta},\end{aligned}\quad (\text{A1})$$

where  $z, r$  and  $\theta$  are the vertical, radial and polar angle coordinates, and

$$\begin{aligned}\hat{\phi} &= \frac{M_0}{4\pi\rho} \frac{2}{\pi} \text{Im} \int_c^{+i\infty+c} \sum_{i=1}^3 C_i(p) A_i(\theta, \lambda, \delta) \frac{p}{\eta_\alpha} \exp(-s\eta_\alpha|z|) K_{3-i}(spr) dp, \\ \hat{\Omega} &= \frac{M_0}{4\pi\rho} \frac{2}{\pi} \text{Im} \int_c^{+i\infty+c} \sum_{i=1}^3 SV_i(p) A_i(\theta, \lambda, \delta) \frac{p}{\eta_\beta} \exp(-s\eta_\beta|z|) K_{3-i}(spr) dp, \\ \hat{\chi} &= \frac{M_0}{4\pi\rho} \frac{2}{\pi} \text{Im} \int_c^{+i\infty+c} \sum_{i=1}^2 SH_i(p) A_{i+3}(\theta, \lambda, \delta) \frac{p}{\eta_\beta} \exp(-s\eta_\alpha|z|) K_{3-i}(spr) dp,\end{aligned}\quad (\text{A2})$$

where  $K_i$  is the modified Bessel function,  $\eta_v = (1/v^2 - p^2)^{1/2}$ ,  $v = \alpha$  for  $P$  waves and  $v = \beta$  for  $S$  waves, and  $i = 1$  for pure strike-slip,  $i = 2$  for dip slip and  $i = 3$  for  $45^\circ$  dip slip, describing the three fundamental fault mechanisms. The factors  $C_i, SV_i, SH_i$  are vertical radiation patterns

$$\begin{aligned}C_1 &= -p^2, \\ SV_1 &= -\varepsilon p \eta_\beta, \\ SH_1 &= 1/\beta^2, \\ C_2 &= 2\varepsilon p \eta_\alpha, \\ SV_2 &= (\eta_\beta^2 - p^2), \\ SH_2 &= -\frac{\varepsilon}{\beta^2} \frac{\eta_\beta}{p}, \\ C_3 &= (p^2 - 2\eta_\alpha^2), \\ SV_3 &= 3\varepsilon p \eta_\beta,\end{aligned}\quad (\text{A3})$$

where  $\varepsilon = \text{sgn}(z)$ , and  $A_i$  are horizontal radiation patterns

$$\begin{aligned}A_1 &= \sin 2\theta \cos \lambda \sin \delta + 1/2 \cos 2\theta \sin \lambda \sin 2\delta, \\ A_2 &= \cos \theta \cos \lambda \cos \delta - \sin \theta \sin \lambda \cos 2\delta, \\ A_3 &= 1/2 \sin \lambda \sin 2\delta, \\ A_4 &= \cos 2\theta \cos \lambda \sin \delta - 1/2 \sin 2\theta \sin \lambda \sin 2\delta, \\ A_5 &= -\sin \theta \cos \lambda \cos \delta - \cos \theta \sin \lambda \cos 2\delta.\end{aligned}\quad (\text{A4})$$

Although these equations can be integrated numerically, a useful approximation is obtained by taking the first term of the asymptotic series, and applying Cagniard–de Hoop theory (Helmberger & Harkrider 1977). In the time domain, the displacement becomes

$$\begin{aligned}W_\alpha &= L^{-1} \left( \frac{\partial \hat{\phi}}{\partial z} \right) = \frac{M_0}{4\pi\rho} \frac{2}{\pi} A_i(\theta, \lambda, \delta) \frac{d}{dt} \left\{ \frac{1}{\sqrt{2r}} \frac{1}{\sqrt{t}} * \text{Im} \left[ C_i(p) \frac{\sqrt{p}}{\eta_\alpha} (-\varepsilon \eta_\alpha) \frac{dp}{dt} \right] \right\}, \\ W_\beta &= L^{-1} \left( sp\hat{\Omega} \right) = \frac{M_0}{4\pi\rho} \frac{2}{\pi} A_i(\theta, \lambda, \delta) \frac{d}{dt} \left\{ \frac{1}{\sqrt{2r}} \frac{1}{\sqrt{t}} * \text{Im} \left[ SV_i(p) \frac{\sqrt{p}}{\eta_\beta} (p) \frac{dp}{dt} \right] \right\}, \\ Q_\alpha &= L^{-1} \left( \frac{\partial \hat{\phi}}{\partial r} \right) = \frac{M_0}{4\pi\rho} \frac{2}{\pi} A_i(\theta, \lambda, \delta) \frac{d}{dt} \left\{ \frac{1}{\sqrt{2r}} \frac{1}{\sqrt{t}} * \text{Im} \left[ C_i(p) \frac{\sqrt{p}}{\eta_\alpha} (-p) \frac{dp}{dt} \right] \right\}, \\ Q_\beta &= L^{-1} \left( -\frac{1}{sp} \frac{\partial \hat{\Omega}}{\partial r \partial z} \right) = \frac{M_0}{4\pi\rho} \frac{2}{\pi} A_i(\theta, \lambda, \delta) \frac{d}{dt} \left\{ \frac{1}{\sqrt{2r}} \frac{1}{\sqrt{t}} * \text{Im} \left[ SV_i(p) \frac{\sqrt{p}}{\eta_\beta} (-\varepsilon \eta_\beta) \frac{dp}{dt} \right] \right\}, \\ V &= L^{-1} \left( -\frac{\partial \hat{\chi}}{\partial r} \right) = \frac{M_0}{4\pi\rho} \frac{2}{\pi} A_{i+3}(\theta, \lambda, \delta) \frac{d}{dt} \left\{ \frac{1}{\sqrt{2r}} \frac{1}{\sqrt{t}} * \text{Im} \left[ SH_i(p) \frac{\sqrt{p}}{\eta_\beta} (p) \frac{dp}{dt} \right] \right\},\end{aligned}\quad (\text{A5})$$

where

$$\begin{aligned} p &= \frac{r}{R^2} t + i \left( t^2 - \frac{R^2}{V^2} \right)^{1/2} \frac{|z|}{R^2}, \\ \eta_v &= \frac{|z|}{R^2} t - i \left( t^2 - \frac{R^2}{V^2} \right)^{1/2} \frac{r}{R^2} \end{aligned} \quad (\text{A6})$$

and  $W_\alpha + W_\beta$  approximates the vertical displacement,  $Q_\alpha + Q_\beta$  approximates the radial displacement and  $V$  approximates the tangential displacement, because the other terms in eq. (A1) are for the near field and thus neglected. However, because these terms involve simple derivatives of the  $P$ - $SV$  and  $SH$  fields, they can also be expanded as power series to recover most of the near field (Helmberger & Harkrider 1977).

In eq. (A5), the term

$$\frac{1}{\eta} \frac{dp}{dt} = \frac{i}{(t^2 - R^2/v^2)^{1/2}} \quad (\text{A7})$$

has a singularity at  $t = R/v$ , the time when the phase arrives. Thus using the first motion approximation, eq. (A6) becomes  $p = p_0 = r/Rv$ , and eq. (A5) can be simplified as

$$\text{Im} \left[ \sqrt{p} (\dots) \frac{1}{\eta} \frac{dp}{dt} \right] \approx \text{Im} \left[ \sqrt{p_0} (\dots) \frac{1}{\eta} \frac{dp}{dt} \right] = \sqrt{p_0} \text{Im} \left[ (\dots) \frac{1}{\eta} \frac{dp}{dt} \right], \quad (\text{A8})$$

where  $\sqrt{p_0}$  is real. Note that without  $\sqrt{p}$  in the equation,  $\text{Im}[\dots]$  satisfies the 2-D wave equation, similar to the term  $V_{2D}$  in eq. (4).

The foregoing deduction is for a homogeneous space, but it can be generalized to flat or dipping layered media using general ray theory (Hong & Helmberger 1977). We can rewrite the displacement as explicit contributions from different fundamental faults, for example  $Q_\alpha = \frac{d}{dt} \left[ \frac{1}{\sqrt{t}} * \sqrt{p_0(t)/r} (\sum_{i=1}^3 A_i Q_\alpha^i) \right]$ , where  $Q_\alpha^i$  and other similar terms are

$$\begin{aligned} Q_\alpha^1(r, z, t) &= r \begin{bmatrix} r^2 - 3 & z^2 + T_\alpha ( & 3 & z^2 ) \end{bmatrix} \Psi_\alpha, \\ Q_\beta^1(r, z, t) &= r \begin{bmatrix} -r^2 + 3 & z^2 + T_\beta ( & r^2 - 2 & z^2 ) \end{bmatrix} \Psi_\beta, \\ W_\alpha^1(r, z, t) &= -z \begin{bmatrix} -3 r^2 + & z^2 + T_\alpha ( 2 & r^2 - & z^2 ) \end{bmatrix} \Psi_\alpha, \\ W_\beta^1(r, z, t) &= -z \begin{bmatrix} 3 & r^2 - & z^2 + T_\beta ( -2 r^2 + & z^2 ) \end{bmatrix} \Psi_\beta, \\ Q_\alpha^2(r, z, t) &= -z \begin{bmatrix} 6 & r^2 - 2 & z^2 + T_\alpha ( -4 r^2 + 2 & z^2 ) \end{bmatrix} \Psi_\alpha, \\ Q_\beta^2(r, z, t) &= -z \begin{bmatrix} -6 r^2 + 2 & z^2 + T_\beta ( 5 & r^2 - & z^2 ) \end{bmatrix} \Psi_\beta, \\ W_\alpha^2(r, z, t) &= r \begin{bmatrix} 2 & r^2 - 6 & z^2 + T_\alpha ( -2 r^2 + 4 & z^2 ) \end{bmatrix} \Psi_\alpha, \\ W_\beta^2(r, z, t) &= r \begin{bmatrix} -2 r^2 + 6 & z^2 + T_\beta ( r^2 - 5 & z^2 ) \end{bmatrix} \Psi_\beta, \\ Q_\alpha^3(r, z, t) &= r \begin{bmatrix} -3 r^2 + 9 & z^2 + T_\alpha ( 2 & r^2 - 7 & z^2 ) \end{bmatrix} \Psi_\alpha, \\ Q_\beta^3(r, z, t) &= r \begin{bmatrix} 3 & r^2 - 9 & z^2 + T_\beta ( -3 r^2 + 6 & z^2 ) \end{bmatrix} \Psi_\beta, \\ W_\alpha^3(r, z, t) &= -z \begin{bmatrix} 9 & r^2 - 3 & z^2 + T_\alpha ( -8 r^2 + & z^2 ) \end{bmatrix} \Psi_\alpha, \\ W_\beta^3(r, z, t) &= -z \begin{bmatrix} -9 r^2 + 3 & z^2 + T_\beta ( 6 & r^2 - 3 & z^2 ) \end{bmatrix} \Psi_\beta, \end{aligned} \quad (\text{A9})$$

where

$$\begin{aligned} T_\gamma &= \frac{R^2}{t^2 \gamma^2}, \\ \Psi_\gamma &= \frac{M_0}{4\pi^2 \rho} \sqrt{2} \frac{t^2}{R^6 \sqrt{1 - T_\gamma}} H(t - R/\gamma) \end{aligned} \quad (\text{A10})$$

for  $P$ - $SV$ , and for  $SH$

$$\begin{aligned} V^4 &= \frac{M_0}{4\pi^2 \rho} \sqrt{2} \frac{r}{R} \frac{1}{\beta^2 R} \frac{1}{\sqrt{1 - T_\beta}} H(t - R/\beta), \\ V^5 &= \frac{M_0}{4\pi^2 \rho} \sqrt{2} \frac{\sqrt{R^2 - r^2}}{R} \frac{1}{\beta^2 R} \frac{1}{\sqrt{1 - T_\beta}} H(t - R/\beta). \end{aligned}$$

Note that  $W_{2D} = W_\alpha^i + W_\beta^i$ ,  $Q_{2D} = Q_\alpha^i + Q_\beta^i$  satisfies the 2-D wave equation, and can be interfaced using 2-D finite differences.

The above formula was derived for cylindrical coordinates. However, it is better to use Cartesian coordinates to obtain a formula suitable for FD source injection (see Fig. 5). Converting from cylindrical coordinates  $\{Q, V, W\}(r, \theta, z)$  to Cartesian coordinates  $\{U_x, U_y, U_z\}(r, \theta, z)$  is straightforward for  $x \geq 0$ , but for  $x < 0$ , it must be noted that the sign convention for displacement changes, and  $\theta = \theta_c + \pi$ . We obtain

$$\begin{aligned} \{U_x, U_y, U_z\}(x, z) &= \{Q, V, W\}(r = x, z, \theta = \theta_c), \quad x \geq 0, \\ \{U_x, U_y, U_z\}(x, z) &= \{-Q, -V, W\}(r = -x, z, \theta = \theta_c + \pi), \quad x < 0. \end{aligned}$$

Thus, for both  $x \geq 0$  and  $x < 0$

$$\{U_x, U_y, U_z\}(x, z) = \{Q, V, W\}(r = x, z, \theta = \theta_c). \quad (\text{A11})$$

Therefore, we only need to change  $r$  to  $x$  in eq. (A9), and use  $\theta = \theta_c$  for both  $x \geq 0$  and  $x < 0$  to obtain a solution in Cartesian coordinates.